INVESTIGATION ON IONICITY AND ITS EFFECT ON CHARGE CARRIER SELECTIVITY FOR N-TYPE CRYSTALLINE SILICON SOLAR CELLS

A THESIS SUBMITTED TO
THE GRADUATE SCHOOL OF NATURAL AND APPLIED SCIENCES
OF
MIDDLE EAST TECHNICAL UNIVERSITY

BY

BASIL MOHAMED MAHMOUD ELDEEB

IN PARTIAL FULFILLMENT OF THE REQUIREMENTS
FOR
THE DEGREE OF MASTER OF SCIENCE
IN
PHYSICS

AUGUST 2022

Approval of the thesis:

INVESTIGATION ON IONICITY AND ITS EFFECT ON CHARGE CARRIER SELECTIVITY FOR N-TYPE CRYSTALLINE SILICON SOLAR CELLS

submitted by **BASIL MOHAMED MAHMOUD ELDEEB** in partial fulfillment of the requirements for the degree of **Master of Science in Physics, Middle East Technical University** by,

Prof. Dr. Halil Kalıpçılar
Dean, Graduate School of **Natural and Applied Sciences** _____

Prof. Dr. Seçkin Kurkcuoglu
Head of the Department, **Physics, METU** _____

Prof. Dr. Raşit Turan
Supervisor, **Physics, METU** _____

Examining Committee Members:

Prof. Dr. Mehmet Parlak
Physics, METU _____

Prof. Dr. Raşit Turan
Physics, METU _____

Assoc. Prof. Dr. Mustafa Kulakcı
Physics, ESTU _____

Date: 31.08.2022

I hereby declare that all information in this document has been obtained and presented in accordance with academic rules and ethical conduct. I also declare that, as required by these rules and conduct, I have fully cited and referenced all material and results that are not original to this work.

Name Last name : Basil Eldeeb

Signature :

ABSTRACT

INVESTIGATION ON IONICITY AND ITS EFFECT ON CHARGE CARRIER SELECTIVITY FOR N-TYPE CRYSTALLINE SILICON SOLAR CELLS

Eldeeb, Basil
Master of Science, Physics
Supervisor : Prof. Dr. Raşit Turan

August 2022, 86 pages

Optoelectronic device performance is not exactly governed by the band alignment between two materials. Interfacial layers in combination with a metal cap dictate charge-carrier selectivity and hence semiconductor device performance. Considering the investigations done on a wide array of solid-state surfaces and heterojunctions done both experimentally and theoretically, it is found that the electron localizability, which is quantifiable through the bandgap energy and band width, plays an integral role in the degree of obeying the Schottky-Mott rule and hence the optoelectronic properties of interfaces. By proposing and utilizing novel ionic crystals (NaF and NaCl) as ultrathin interfacial layers between Aluminum and n-type silicon, we demonstrate Fermi-level unpinning and show contacts having an effect similar to that of heavily doping the surface of silicon. We managed to achieve 17.3% efficiency for NaF with suboptimal passivation. For planar interfaces, a strategy for contacts is proposed for enhancing electron transport across boundaries.

Keywords: Ionicity, Tunneling, Charge-carrier-selectivity, Schottky barrier.

ÖZ

N-TİPİ KRİSTAL SİLİKON GÜNEŞ HÜCRELERİ İÇİN İYONİKLİK VE YÜK TAŞIYICI SEÇİMİ ÜZERİNE ETKİSİNİN İNCELENMESİ

Eldeeb, Basil
Yüksek Lisans, Fizik
Tez Yöneticisi: Prof. Dr. Raşit Turan

Ağustos 2022, 86 sayfa

Optoelektronik cihaz performansı, iki malzeme arasındaki bant hizalaması tarafından yönetilir. Metal bir kapak ile birlikte arayüzey katmanları, yük taşıyıcı seçiciliğini ve dolayısıyla yarı iletken cihaz performansını belirler. Hem deneysel hem de teorik olarak çok çeşitli katı hal yüzeyleri ve heteroeklemler üzerinde yapılan araştırmalar göz önüne alındığında, bant aralığı enerjisi ve bant genişliği ile ölçülebilen elektron yerelleştirilebilirliğinin, kurallara uyma derecesinde ayrılmaz bir rol oynadığı bulunmuştur. Schottky-Mott kuralı ve dolayısıyla arayüzlerin optoelektronik özellikleri. Alüminyum ve n-tipi silikon arasında ultra ince ara yüzey katmanları olarak yeni iyonik kristalleri (NaF ve NaCl) önererek ve kullanarak, Fermi düzeyinde sabitlemeyi ve silikon yüzeyini yoğun bir şekilde dopinge benzer bir etkiye sahip temasları gösterdik. Optimalin altında pasifleştirme ile NaF için %17,3 verimlilik elde etmeyi başardık. Düzlemsel arayüzler için, sınırlar arasında elektron taşınmasını arttırmak için temaslar için bir strateji önerilmiştir.

Anahtar Kelimeler: İyoniklik, Tünelleme, Yük taşıyıcı seçicilik, Schottky engeli.

أَعُوذُ بِاللَّهِ مِنَ الشَّيطَانِ الرَّجِيمِ

ٱلْحَمْدُ لِلَّهِ ٱلَّذِى خَلَقَ ٱلسَّمَـٰوَٰتِ وَٱلْأَرْضَ وَجَعَلَ ٱلظُّلُمَـٰتِ وَٱلنُّورَ ۖ

ثُمَّ ٱلَّذِينَ كَفَرُوا۟ بِرَبِّهِمْ يَعْدِلُون

[الأنعام: 1]

ACKNOWLEDGMENTS

First and foremost, I would like to thank my family for financing my existence, raising me, and supporting me in hardship and wealth. The debt that I owe you is unfathomable. May Allah assist me in paying some of it and in making you proud.

I would like to thank Prof. Dr. Rasit Turan for supporting my work and advising me on the various issues I faced throughout the MSc program both academic and personal. I would like to thank my supervisor Dr. Hisham Nasser, Dr. İbrahim Murat Öztürk, Dr. Mona Zolfaghari Borra, Konstantin Tsoi, and Tunç Bektaş, for teaching me how to use the various tools and chemical processes I needed to better my understanding of semiconductor technology.

I would like to thank Ahmed Halawa, Ahmed Sameh Saafan, Batuhan Erol, Loay Akmal Madbouly, Mohamed Adli Ayesh, Omar Mustafa Qawas, and Tarek Elsebaei for encouragement, support, and philosophical discussions that helped me push through and widen my perspective on (meta)physical matters.

This work was partially funded by Scientific and Technological Research Council of Turkey (TUBITAK) under grant number 119N339.

TABLE OF CONTENTS

CHAPTER 1

INTRODUCTION

Electric phenomenon, arguably, was first mentioned in writing by the ancient Greeks in its electrostatic form: rubbing amber (called electron in ancient Greek) against animal fur later causes the amber to attract certain objects like feathers. Even the sun's name in ancient Greek was elector; now, we are researching how to maximize our cultivation of electricity from Elector. Almost concurrently, magnetic phenomenon was first mentioned by Thales of Miletus (south of present-day Izmir, Turkey) around 600 B.C.. Almost two thousand years later, before Newton's invention/use of mathematics to predict Halley's comet's trajectory, W. Gilbert started studying amber and electricity and others studied the lodestone [1]. After almost three centuries of observations and experimentation, J.C. Maxwell had established that any electromagnetic phenomenon can be described by five simple equations (the, famously named, Maxwell's equations and the Lorentz force equation) and the fact that light is an electromagnetic phenomenon. Around the same time, rectifying current response to electric potential difference was discovered by F. Braun [2].

In 1905, Albert Einstein used Max Planck's concept of quantization of energy, that solved the UV catastrophe, to explain the photoelectric effect, revealing the quantum nature of electromagnetic phenomena. Soon after, quantum mechanics was used to describe other macroscopic phenomena, including the rectifying current response, that cannot be explained by classical statistical mechanics.

Till the advent of quantum mechanics, the only manner by which electricity was generated was through exhausting an exothermic fuel to evaporate water where the vapor is used to constantly change a strong magnet's relative position (flux density)

to wires such that the change in flux results in an electric current, inspired by Faraday's observations. Using quantum mechanics, we can understand the behaviour of electrons such that we can generate electricity by placing a sub-millimeter "slab" (solar cell) under the sun. The question becomes: how does this occur and how do we maximize the electricity generation and extraction?

Classically, the discontinuity of matter gives rise to surfaces that can be described by boundary conditions such that the electic and magnetic fields must act accordingly [3]. Depending on the charge density of the matter, electromagnetic fields could either propagate within the material or be forbidden from moving more than a few nanometers, such is the case of dielectrics and metals, respectively. Which is why we can see through one form of matter and not the other. This was studied from a macroscopic perspective up to the beginning of the 20^{th} century. The nanoscopic and quantum mechanical perspectives of matter and the discovery of semiconductors gave rise to technology as we know it. In this context, our understanding of matter changed.

The main motivation behind this thesis is the fact that inserting an ultrathin (on the order of a few nanometers) ionic crystal between a metal and a semiconductor enhances the electric transport across the interface such that the configuration is comparable, in performance, to heavily doping the surface of Si then contacting it with a metal. To our knowledge, this was first demonstrated by L.S. Hung et al. in 1997 [4]. Later, the device structure was studied under different circumstances from different perspectives. Afterwards, J. Bullock et al. demonstrated photovoltaic conversion efficiencies of 19% [5] by utilizing Al/LiF_x ($x < 1$) and, later, 20.7% [6] by using, both, Al/LiF_x ($x < 1$) and Ag/MoO_x ($x < 3$) contacts for charge collection in crystalline silicon (c-Si) solar cells (without surface doping). By employing other contact strategies, (texturing at the front and passivation by dielectric layers) the efficiency reached 23% [7]. Later, researchers went in a similar direction to optimize contacts beyond surface doping c-Si [8]–[14].

Thus, the concern of this thesis is to accumulate the models and studies done on crytalline surfaces. Another concern is to understand the effect of the arising different

phenomena manifesting due to contacting different crystals on the electrical properties of contacts with an application on silicon (Si)-based photovoltaic cells.

1.1 Solids

Categorizing and modelling solids started with the start of humanity. It was simple; mechanically, one solid broke/dented the other. Optically, one solid was shiny, the other was not (opaque). After millennia of investigation, we are at the stage of describing/categorizing solids by their electrons' environment (work function) [15] (more generally, band theory). Briefly, band theory describes how discrete energy levels, that are found by solving the Schrodinger equation of a single electron in a potential well, are perturbed and split by constructing solids atom by atom [16]. Thus, in a solid with Avogadro's number of atoms, each discrete level turns to a band of almost infinitesimally spaced levels. In some solids, bands overlap (some metals), and in most, they repel one another forming bandgaps.

As the electron is categorized as a fermion, which is a particle with half-integral spin, it obeys Fermi-Dirac (FD) statistics. Soon after the development of FD statistics, A. Sommerfeld proposed to use it to describe macroscopic phenomena of metals, such as conductivity and heat capacitance [17]. Although, the first motivation was to describe metals, one could apply FD statistics to any system of electrons and ascribe the system a Fermi-level (FL). The FL describes the probability of electrons occupying energy levels below it in a continuum of allowed states. The FL of an intrinsic solid will always be situated near the midgap [17]. The location of the FL could be changed relative to its intrinsic location by doping, which is the controlled addition of elements either having more or less valence electrons than the host solid [16]. Another manner by which the FL could change its location is through defects, which mainly occurs at the surface [18].

1.2 Junctions

A junction, in the context of solid-state physics, is defined as the physical contact between two solids. When both solids are the same and differ in majority charge-carrier concentration, the junction is referred to as a homojunction or a PN junction. Other junctions are referred to as heterojunctions.

1.2.1 The PN Junction

Starting with the simplest type of junction: two intrisically identical semiconductors with different doping type, (n)egative-type and (p)ositive-type. In this case, the FL on the p-doped side will be lower than the intrinsic level, E_i, while on the n-doped side it will be at a relatively higher position. Upon contact, thermodynamic equilibrium dictates that the FL be constant throughout the interface [16].

1.2.2 The Metal/Semiconductor (MS) Junction:

For the ideal MS junction, W. Schottky proposed that an electron would experience an energy barrier corresponding to the difference between the metal (M) work function (ϕ_M) and the electron affinity (χ) of the semiconductor (S) when transporting from M to S such that the potential barrier that an electron experiences from the metal side is:

$$\phi_B = \phi_M - \chi$$

where ϕ_B is the Schottky barrier height (SBH), this is the Schottky-Mott rule for n-type semiconductors [16]. Under forward bias, the barrier diminishes, while in reverse bias, the depletion region increases in width such that it is increasingly difficult for electrons to cross from M to S. The formulation does not impose an upper limit on the size of the bandgap energy, such that it should be capable of describing any metal/non-metal junction. However, numerous experiments revealed

that the barrier is insensitive to ϕ_M and surface orientation for many semiconductors, especially Si and germanium (Ge) [2].

However, as real crystals are not infinite in space, the concept of the forbidden region is not completely valid at the edge of a crystal where some neighbors are missing (technically, an infinite number of neighbors is missing, however due to screening effects, an ion's perception of neighbors exponentially decays with each cascading neighbor). This causes some charge transfer between the surface and the bulk of the crystal to render the surface neutral [19]. Such effect, among others, was not accounted for in W. Schottky's formulation. This is the main reason why the Schottky-Mott's rule is not applicable in most interfaces.

Since photovoltaic solar cells are PN junctions contacted with a metal, understanding the MS interface is paramount to maximizing the efficiency of such devices and other optoelectronics-based devices. Therefore, after a literature review, we tested sodium chloride (NaCl) and sodium fluoride (NaF) as interfacial layers (ILs) on different substrates with different metals to gain a better understanding of what ionic crystals do in such regime. We observed Fermi level unpinning when using such layers between c-Si and different metals (i.e., the thermionic barrier highly depends on the metal's work function). Then, we measured the contact resistivity of the ionic crystals for different thicknesses, in nanometers, to see their viability for future solar cell applications. LiF was studied first, to reproduce literature results, such that we could compare the performance of the layers in the simple contact schemes (planar and textured).

CHAPTER 2

THEORY & LITERATURE REVIEW

Although, optical and electronic properties of interfaces are the most relevant in device physics, they remain elusive in nature. This is reflected in the several proposed theories from Fowler-Nordheim theory of cold emission (Metal/Vacuum) [20], and its corrections for image effect [21], to Schottky/Mott models for MS contacts and Bethe's theory of thermionic emission [2] (metal/non-metal), to the various models that account for the lack of predictability of Schottky's theory due to the Fermi level pinning (FLP) (Bardeen's interface states [18], The S-Parameter [22], and Metal-Induced Gap States (MIGS)) [23]. Some of these models are qualitative, while others are quantitative with limited success. As R. Tung mentioned (who also contributed with a theory of inhomogeneous barriers at the interface [24], [25]); the Schottky Barrier Height (SBH) is a multidisciplinary phenomenon, ranging from quantum mechanics to chemistry and engineering, which keeps it shrouded in mystery for almost a century. There are even different reports on the work function of noble metals e.g., for Au, in the 80s, its work function was reported as 4.7-4.8eV yet, currently it is reported as 5.1-5.3eV [2], [26], [27]. This, among other factors, further complicates the understanding of the SBH and FLP phenomena. It was reported that even the vacuum chamber usage history altered interface parameters significantly, however reproducible [28].

As companies do not need exact physics to demonstrate and produce repeatable solid-state devices, especially transistors, a combination of precise calibration and a device construction recipe are all that is needed for technology to reach the current level at which we see it, as technology relies on the identical performance of billions of components (e.g., transistors) whose only job is either pass or block current.

Since Moore's law reached its limit, the next generation devices will possess a high surface to volume ratio. This necessitates the exact understanding of surface phenomena, electronically, as their contributions to new devices will be substantial, especially in regard to 2D transistors [29] and spin-based devices and their integration with current solid-state devices within nanoscopic volumes.

2.1 Theory

In order to understand the phenomena occurring at the surface of matter, we ought to start from the ideal state of an infinite solid and then look at the surface. In order to do that, we must describe the environment an electron perceives in an infinite solid. This can be done by using the Schrödinger equation, as the electron is a quantum particle, with the appropriate boundary conditions.

2.1.1 Modelling Solids

When a solid is viewed from a classical point of view, the Drude model, it fails to predict many features of almost all metals, not to mention other solids, such as: the sign in the Hall coefficient, mean square electronic speed, electronic contribution to heat capacity [17] (p.21-25). This is due to the faulty assumptions used:

- All valence electrons are detached from the mother ion (only valid for metals).
- Ions' role in physical phenomena is ignored, other than maintaining charge neutrality.
- Electron-electron interactions are ignored.
- Conduction electrons obey the classical Maxwell-Boltzmann statistics.

Sommerfeld's model used Fermi-Dirac (FD) statistics, which fixed some features. This quickly established the undeniable quantum nature of solids. However, since Sommerfeld did not change the other assumptions, it still failed to account for many

observations. One can see a list of failed predictions in [17] (p.58-60). Both models are usually referred to as "the free electron model".

Seeing that the classical description fails and simply using FD statistics does not work for almost all solids. We need to use the Schrödinger equation. We start by describing how an electron is moving when it is surrounded by nothing, i.e. when an electron is in vacuum. The general Schrodinger equation (SE) is:

$$\hat{H}\psi = \left(\frac{\hat{p}^2}{2m} + U(\boldsymbol{r})\right)\psi = E\psi$$

(2.1)

where $\hat{p}$ is the momentum operator and V is the potential, becomes

$$\hat{H}\psi = \frac{\hat{p}^2}{2m}\psi = E\psi$$

(2.2)

as there is no potential in vacuum. In this case, the energy of an electron is arbitrary, it can be moving at any speed depending on the observer. In order to describe electron behavior, one must properly describe the environment in which they reside which is summarized in the potential term U. Solids tend to form crystals, which are periodic structures composed of ions situated at Bravais lattice points (which are points that can be defined by primitve vectors, $\mathbf{a}_i$, and generated by translation vectors). The size of the crystal can vary from nanometers to centimeters, in range, all having different applications. Bloch's theorem takes advantage of the structure and states that given a periodic potential, the electron wavefunction ψ, as a function of space, for all Bravais lattice vector **R**, obey:

$$\psi(\boldsymbol{r} + \boldsymbol{R}) = \psi(\boldsymbol{r})e^{i\boldsymbol{k}.\boldsymbol{R}}$$

or

$$\psi_{n\boldsymbol{k}}(\boldsymbol{r}) = e^{i\boldsymbol{k}.\boldsymbol{r}}u_{n\boldsymbol{k}}(\boldsymbol{r})$$

(2.3)

For a given wave vector $\boldsymbol{k} = x_i\boldsymbol{b}_i$ ($\boldsymbol{b}_i\boldsymbol{a}_j = 2\pi\delta_{ij}$) where u(**r**) has the periodicity of the lattice (i.e. $u_{n\boldsymbol{k}}(\boldsymbol{r}) = u_{n\boldsymbol{k}}(\boldsymbol{r} + \boldsymbol{R})$). The index n can be understood as follows: as isolated atoms, having discrete electronic energy levels labeled n, are brought to

form a crystal, the discrete levels form a band of continuous levels, satisfying the SE for a given **k** value. When we apply Bloch's theorem to the Born-Von Karman (BVK) boundary conditions:

$$\psi(\boldsymbol{r} + N_i \boldsymbol{a}_i) = \psi(\boldsymbol{r}) \tag{2.4}$$

Where N_i are the number of primitive cells in each direction such that $N=N_1N_2N_3$ is the total number of primitive cells in the volume under study. This leads us to:

$$\exp(iN_i \boldsymbol{k}.\boldsymbol{a}_i) = 1 \tag{2.5}$$

$$N_i x_i b_i a_j = 2\pi m, \text{ where m=1,2,3,....}$$

$$x_i = {}^{m_i}/_{N_i} \tag{2.6}$$

The coefficients x_i show that allowed **k** values become continuous in the limit of infinite volume. Looking for the Bloch solutions to the SE for a periodic potential U(**r**) (=U(**r**+**R**)), under BVK boundary condition for a given a given **k**:

$$H\psi_{n\boldsymbol{k}} = e^{i\boldsymbol{k}.\boldsymbol{r}} H_{\boldsymbol{k}} u_{n\boldsymbol{k}}(\boldsymbol{r}) \tag{2.7}$$

Where,

$$H_{\boldsymbol{k}} u_{\boldsymbol{k}}(\boldsymbol{r}) = [\frac{\hbar^2}{2m}\left(\frac{1}{i}\nabla + k\right)^2 + U(\boldsymbol{r})] u_{\boldsymbol{k}}(\boldsymbol{r}) = \varepsilon_{\boldsymbol{k}} u_{\boldsymbol{k}}(\boldsymbol{r}) \tag{2.8}$$

Thus, for a given **k** there is a family of eigenvalues $\varepsilon_{n,\boldsymbol{k}} \equiv \varepsilon_n(\boldsymbol{k})$. For a given n, the wavefunction and eigenvalues are periodic functions of **k** in the reciprocal lattice vector (RLV) **K** defined by **R** (**K.R**=2πm, where m=1,2,3,…):

$$\psi_{n,\boldsymbol{k}+\boldsymbol{K}}(\boldsymbol{r}) = \psi_{n\boldsymbol{k}}(\boldsymbol{r})$$

$$\varepsilon_{n,\boldsymbol{k}+\boldsymbol{K}} = \varepsilon_{n\boldsymbol{k}} \tag{2.9}$$

When ε_n is plotted against **k** we arrive at the band structure of the crystalline solid. The wavefunction obeying the BVK boundary condition can always be expanded as the set of all plane waves satisfying the boundary condition:

$$\psi_{n,\boldsymbol{k}}(\boldsymbol{r}) = \sum_{\boldsymbol{q}} c_{\boldsymbol{q}} e^{i\boldsymbol{q}.\boldsymbol{r}}$$

(2.10)

Where it can shown that **q=k-K**. The kinetic energy term gives:

$$-\frac{\hbar^2}{2m}\nabla^2\psi = \frac{\hbar^2}{2m}\sum_{\boldsymbol{k}-\boldsymbol{K}}(\boldsymbol{k}-\boldsymbol{K})^2 c_{\boldsymbol{k}-\boldsymbol{K}} e^{i(\boldsymbol{k}-\boldsymbol{K}).\boldsymbol{r}}$$

(2.11)

As for the periodic potential:

$$U(\boldsymbol{r}) = \sum_{\boldsymbol{k}} U_{\boldsymbol{k}}\, e^{i\boldsymbol{k}.\boldsymbol{r}} = \sum_{\boldsymbol{K}} U_{\boldsymbol{K}} e^{i\boldsymbol{K}.\boldsymbol{r}}$$

(2.12)

As $U_{\boldsymbol{k}}$ is only nonvanishing when **k** is a RLV. Operating with the potential on the wavefunction, we get:

$$U\psi = \sum_{\boldsymbol{K}} U_{\boldsymbol{K}} e^{i\boldsymbol{K}.\boldsymbol{r}} \sum_{\boldsymbol{k}-\boldsymbol{K}'} c_{\boldsymbol{k}-\boldsymbol{K}'} e^{i(\boldsymbol{k}-\boldsymbol{K}').\boldsymbol{r}}$$

$$U\psi = \sum_{\boldsymbol{K},\boldsymbol{k}-\boldsymbol{K}'} U_{\boldsymbol{K}} c_{\boldsymbol{k}-(\boldsymbol{K}'-\boldsymbol{K})} e^{i(\boldsymbol{k}-(\boldsymbol{K}'-\boldsymbol{K}).\boldsymbol{r}}$$

(2.13)

Changing the index from **K'-K** to **K',** the SE becomes:

$$\sum_{\boldsymbol{k}-\boldsymbol{K}} e^{i(\boldsymbol{k}-\boldsymbol{K}).\boldsymbol{r}}\{\frac{\hbar^2}{2m}(\boldsymbol{k}-\boldsymbol{K})^2 c_{\boldsymbol{k}-\boldsymbol{K}} - \sum_{\boldsymbol{K}'} U_{\boldsymbol{K}'-\boldsymbol{K}} c_{\boldsymbol{k}-\boldsymbol{K}'}\} = \sum_{\boldsymbol{k}-\boldsymbol{K}} \varepsilon c_{\boldsymbol{k}-\boldsymbol{K}} e^{i(\boldsymbol{k}-\boldsymbol{K}).\boldsymbol{r}}$$

$$\sum_{\boldsymbol{k}-\boldsymbol{K}} e^{i(\boldsymbol{k}-\boldsymbol{K}).\boldsymbol{r}}\{[\frac{\hbar^2}{2m}(\boldsymbol{k}-\boldsymbol{K})^2 - \varepsilon] c_{\boldsymbol{k}-\boldsymbol{K}} - \sum_{\boldsymbol{K}'} U_{\boldsymbol{K}'-\boldsymbol{K}} c_{\boldsymbol{k}-\boldsymbol{K}'}\} = 0$$

(2.14)

The expression within the parantheses must seperately vanish as the plane waves satisfying BVK form an orthogonal set. Therefore the SE in k-space for allowed **k**:

$$[\frac{\hbar^2}{2m}(\boldsymbol{k}-\boldsymbol{K})^2 - \varepsilon] c_{\boldsymbol{k}-\boldsymbol{K}} - \sum_{\boldsymbol{K}'} U_{\boldsymbol{K}'-\boldsymbol{K}} c_{\boldsymbol{k}-\boldsymbol{K}'} = 0$$

(2.15)

This equation is quite general, as the form of the potential is not even expressed. However, one can still gain insight. In the free-electron case, all $U_{\boldsymbol{K}}$ are zero. Then we have:

$$[\varepsilon^0_{\boldsymbol{k-K}} - \varepsilon] c_{\boldsymbol{k-K}} = 0$$

(2.16)

Where,

$$\varepsilon^0_{\boldsymbol{k-K}} \equiv \frac{\hbar^2}{2m} (\boldsymbol{k} - \boldsymbol{K})^2$$

(2.17)

(2.17) can be regarded as the energy of a free electron moving in a Braivais lattice devoid of potential. (2.16) can be valid in two ways: $c_{\mathbf{k-K}}$ is zero or $\varepsilon = \varepsilon^0_{\boldsymbol{k-K}}$. The first possibility is trivial. The latter may occur in two different ways: there is only one **K** for which $\varepsilon = \varepsilon^0_{\boldsymbol{k-K}}$ is true, unless there are multiple **K** where $\varepsilon^0_{\boldsymbol{k-K}}$ are equal. If there is no degeneracy, then we have:

$$\varepsilon = \varepsilon^0_{\boldsymbol{k-K}}, \ \psi_{\boldsymbol{k}} \propto e^{i(\boldsymbol{k-K}).\boldsymbol{r}}$$

(2.18)

For the degenerate case, there is a set of RLVs $\mathbf{K}_1,\ldots,\mathbf{K}_n$ all corresponding to the same energy. Then, the choice of cofficients $c_{\mathbf{k-K}}$ becomes arbitrary.

Considering the case where the potential is nonzero and weak. This case corresponds to most metals. There will be two cases, again:

One: where the considered energy levels are not degenerate. This can be expressed as follows: fix **k** and consider a particular RLV $\mathbf{K}_1$ such that the free electron energy $\varepsilon^0_{\boldsymbol{k-K_1}}$ is far from the values corresponding to other **K** compared with U:

$$\left|\varepsilon^0_{\boldsymbol{k-K_1}} - \varepsilon^0_{\boldsymbol{k-K}}\right| \gg U, \qquad for\ \boldsymbol{K} \neq \boldsymbol{K_1}$$

Setting $\mathbf{K}=\mathbf{K}_1$ in (2.15):

$$[\varepsilon - \varepsilon^0_{\boldsymbol{k-K_1}}] c_{\boldsymbol{k-K_1}} = \sum_{\boldsymbol{K}} U_{\boldsymbol{K-K_1}} c_{\boldsymbol{k-K}}$$

(2.19)

Since the potential is unique up to a constant, $U_{\mathbf{K}}$ can be set to zero for $\mathbf{K}=0$. For $\mathbf{K}\neq\mathbf{K}_1$ we have:

$$c_{\boldsymbol{k-K}} = \frac{U_{\boldsymbol{K_1-K}} c_{\boldsymbol{k-K_1}}}{\varepsilon - \varepsilon^0_{\boldsymbol{k-K}}} + \sum_{\boldsymbol{K' \neq K_1}} \frac{U_{\boldsymbol{K'-K_1}} c_{\boldsymbol{k-K'}}}{\varepsilon - \varepsilon^0_{\boldsymbol{k-K}}}$$

(2.20)

In the case of no near degeneracy, the denominator will always be an order of magnitude higher than U, thus:

$$c_{\boldsymbol{k-K}} = \frac{U_{\boldsymbol{K_1-K}} c_{\boldsymbol{k-K_1}}}{\varepsilon - \varepsilon^0_{\boldsymbol{k-K}}} + O(U^2)$$

(2.21)

Plugging this into (2.19), we get:

$$[\varepsilon - \varepsilon^0_{\boldsymbol{k-K_1}}] c_{\boldsymbol{k-K_1}} = \sum_{\boldsymbol{K}} \frac{U_{\boldsymbol{K-K_1}} U_{\boldsymbol{K_1-K}} c_{\boldsymbol{k-K_1}}}{\varepsilon - \varepsilon^0_{\boldsymbol{k-K}}} + \ O(U^3)$$

(2.22)

Since the Hamiltonian is real and a set of coordinates can chosen such that the crystal possesses inversion symmetry ($U(\boldsymbol{r}) = U(-\boldsymbol{r})$):

$$U_{\boldsymbol{K}} = U_{\boldsymbol{-K}} = U^*_{\boldsymbol{K}}$$

(2.23)

Then the energy can be expressed as:

$$\varepsilon = \varepsilon^0_{\boldsymbol{k-K_1}} + \sum_{\boldsymbol{K}} \frac{\left|U_{\boldsymbol{K-K_1}}\right|^2}{\varepsilon^0_{\boldsymbol{k-K_1}} - \varepsilon^0_{\boldsymbol{k-K}}} + \ O(U^3)$$

(2.24)

So up to the second order in U, the perturned energy level is shifted by a small negligible quantity since the potential is already taken to be weak. In the case of near degeneracy, we have m levels whose difference is within the first order in U, however, they are far from the other $\varepsilon^0_{\boldsymbol{k-K}}$ on the scale of U:

$$\left|\varepsilon^0_{\boldsymbol{k-K_1}} - \varepsilon^0_{\boldsymbol{k-K_i}}\right| \gg U, i = 1, \dots, m, \boldsymbol{K} \neq \boldsymbol{K_i}$$

(2.25)

This gives rise to m equations that need to be solved, in 1D, m can be at most 2, however, in 3D, it can be a large number. We have:

$$[\varepsilon - \varepsilon^0_{\boldsymbol{k-K_i}}] c_{\boldsymbol{k-K_i}} = \sum_{j=1}^{m} U_{\boldsymbol{K_j-K_i}} c_{\boldsymbol{k-K_j}} + \sum_{\boldsymbol{K} \neq \boldsymbol{K_1}, \dots, \boldsymbol{K_m}} U_{\boldsymbol{K-K_i}} c_{\boldsymbol{k-K}} \ , i = 1, \dots, m$$

(2.26)

For the remaining levels, using (2.15):

$$c_{k-K} = \frac{1}{[\varepsilon - \varepsilon^0_{k-K}]}\left(\sum_{j=1}^{m} U_{K_j-K_i} c_{k-K_j} + \sum_{K \neq K_1,\ldots,K_m} U_{K'-K_i} c_{k-K'}\right), \boldsymbol{K \neq K_i}$$

(2.27)

Since $c_{k-K} \propto U$ when $\boldsymbol{K \neq K_i}$, (2.27) becomes

$$c_{k-K} = \frac{1}{[\varepsilon - \varepsilon^0_{k-K}]}\sum_{j=1}^{m} U_{K_j-K_i} c_{k-K_j} + O(U^2)$$

(2.28)

Putting this in (2.22),

$$[\varepsilon - \varepsilon^0_{k-K_i}] c_{k-K_i} = \sum_{j=1}^{m}\{ U_{K_j-K_i} c_{k-K_j} + (\sum_{K \neq K_1,\ldots,K_m} \frac{U_{K-K_i} U_{K_j-K}}{\varepsilon - \varepsilon^0_{k-K}} c_{k-K_j}) + O(U^3) \}$$

(2.29)

The shift for the nearly degenerate case is approximately of order U, if we ignore the second and third terms, as they are mearly corrections. This implies that that the perturbed levels (an electron moving in a periodic structure relative to one that is moving in free space) a shifted from above and below by U:

$$[\varepsilon - \varepsilon^0_{k-K_i}] c_{k-K_i} \cong \sum_{j=1}^{m}\{ U_{K_j-K_i} c_{k-K_j} \}$$

(2.30)

Looking at the case of m=2; the m equations reduce to:

$$[\varepsilon - \varepsilon^0_{k-K_1}] c_{k-K_1} \cong U_{K_2-K_1} c_{k-K_2}$$
$$[\varepsilon - \varepsilon^0_{k-K_2}] c_{k-K_2} \cong U_{K_1-K_2} c_{k-K_1}$$

(2.31)

Since we decided that U_0=0. Using $\mathbf{q=k-K_1}$ and $\mathbf{K=K_2-K_1}$ we can write the equations as such:

$$[\varepsilon - \varepsilon^0_{q}] c_{q} \cong U_K c_{q-K}$$
$$[\varepsilon - \varepsilon^0_{q-K}] c_{q-K} \cong U_{-K} c_q = U^*_K c_q$$

(2.32)

Since we are assuming that the levels are nearly degenerate, we have:

$$\varepsilon_{\boldsymbol{q}} - \varepsilon^0_{\boldsymbol{q-K}} \cong 0, \left|\varepsilon_{\boldsymbol{q}} - \varepsilon^0_{\boldsymbol{q-K'}}\right| \gg U, for\ \boldsymbol{K'} \neq \boldsymbol{K}$$

(2.33)

The assertion that only the single value of $\boldsymbol{K'} = \boldsymbol{K}$ makes $\varepsilon_{\boldsymbol{q}} = \varepsilon^0_{\boldsymbol{q-K}}$ requires that $|\boldsymbol{q}| = |\boldsymbol{q'}| = |\boldsymbol{q} - \boldsymbol{K}|$ which is the condition for elastic scattering; squaring both sides:

$$q^2 = q^2 + K^2 - 2\boldsymbol{q}.\boldsymbol{K}$$

$$\boldsymbol{K}.\boldsymbol{K} = 2\boldsymbol{q}.\boldsymbol{K}$$

$$\boldsymbol{K}.\widehat{\boldsymbol{K}} = 2\boldsymbol{q}.\widehat{\boldsymbol{K}} = K$$

The condition can be written as:

$$\frac{1}{2}K = \boldsymbol{q}.\widehat{\boldsymbol{K}}$$

(2.34)

This amounts to requiring that **q** lie on the Bragg plane defined by **K/2**. The plane is called a Bragg plane, because he and his son were the ones to identify enhanced reflections at certain angles when X-ray was directed towards macroscopically crystalline solids which was accounted for by regarding the crystal to be made of parallel planes of ions, for which he and his son received the Nobel prize. His formulation forms the basis for identifying crystal orientations and lattice constants through XRD. More on that in the related section. Equations (2.32) have a solution when the determinant is zero:

$$\begin{vmatrix} \varepsilon - \varepsilon^0_{\boldsymbol{q}} & -U_{\boldsymbol{K}} \\ -U^*_{\boldsymbol{K}} & \varepsilon - \varepsilon^0_{\boldsymbol{q-K}} \end{vmatrix} = 0$$

$$\left(\varepsilon - \varepsilon^0_{\boldsymbol{q}}\right)\left(\varepsilon - \varepsilon^0_{\boldsymbol{q-K}}\right) = |U_{\boldsymbol{K}}|^2$$

$$\varepsilon^2 - \left(\varepsilon^0_{\boldsymbol{q}} + \varepsilon^0_{\boldsymbol{q-K}}\right)\varepsilon + \varepsilon^0_{\boldsymbol{q}}\varepsilon^0_{\boldsymbol{q-K}} - |U_{\boldsymbol{K}}|^2 = 0$$

$$\varepsilon = \frac{\left(\varepsilon^0_{\boldsymbol{q}} + \varepsilon^0_{\boldsymbol{q-K}}\right)}{2} \pm \left[\frac{1}{4}\left(\varepsilon^0_{\boldsymbol{q}} + \varepsilon^0_{\boldsymbol{q-K}}\right)^2 - \left(\varepsilon^0_{\boldsymbol{q}}\varepsilon^0_{\boldsymbol{q-K}} - |U_{\boldsymbol{K}}|^2\right)\right]^{1/2}$$

$$\varepsilon = \frac{\left(\varepsilon^0_{\boldsymbol{q}} + \varepsilon^0_{\boldsymbol{q-K}}\right)}{2} \pm \left[\frac{1}{4}\left(\varepsilon^{0\,2}_{\boldsymbol{q}} + \varepsilon^{0\,2}_{\boldsymbol{q-K}} + 2\varepsilon^0_{\boldsymbol{q}}\varepsilon^0_{\boldsymbol{q-K}}\right) - \varepsilon^0_{\boldsymbol{q}}\varepsilon^0_{\boldsymbol{q-K}} + |U_{\boldsymbol{K}}|^2\right]^{1/2}$$

$$\varepsilon = \frac{(\varepsilon_{\boldsymbol{q}}^0 + \varepsilon_{\boldsymbol{q}-\boldsymbol{K}}^0)}{2} \pm \left[\frac{1}{4}\left(\varepsilon_{\boldsymbol{q}}^0 - \varepsilon_{\boldsymbol{q}-\boldsymbol{K}}^0\right)^2 + |U_{\boldsymbol{K}}|^2\right]^{1/2}$$

(2.35)

The roots ε give the main (higher orders in U are less significant) shifts caused by the periodic potential on the free electron energy levels $\varepsilon_{\boldsymbol{q}}^0$ and $\varepsilon_{\boldsymbol{q}-\boldsymbol{K}}^0$ when **q** is close to the Bragg plane at **K**/2, corresponding to near degeneracy. When **q** is exactly on the Bragg plane, the free electron levels become identical and the roots become:

$$\varepsilon = \varepsilon_{\boldsymbol{q}}^0 \pm |U_{\boldsymbol{K}}|$$

(2.36)

Such that the difference between the nearly identical levels become $2|U_{\boldsymbol{K}}|$. This can be regarded as an indirect manifestation of Pauli's exclusion principle; no two electrons can be in the same exact quantum state. Even nearly identical levels "repel" each others' existence such that they are modified.

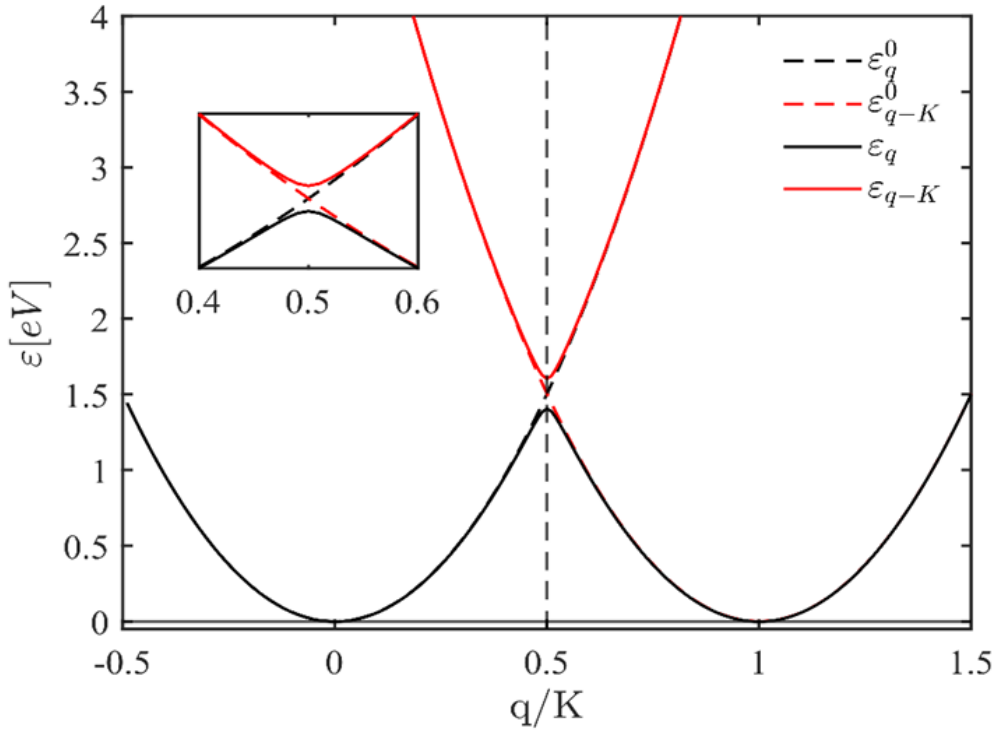

Figure 2.1 The band structure of a 1D periodic structure. Here, we plot the 2 free electron energy levels for wave vectors q and q-K, signified by the dashed lines, along with the perturbed versions, signified by the solid lines. The inset shows the bands near degeneracy, where the potential strength is 0.1eV causing a bandgap of 0.2eV. The energy scale is mainly dictated by the lattice constant chosen, which was 5 angstroms, so in some sense it is arbitrary in this demonstration of near degeneracy.

Looking at Figure 2.1. We see, in the inset, how the $\varepsilon_{\boldsymbol{q}}^{0}$ band starts deviating -around a difference $U_{\mathbf{K}}$ from $\varepsilon_{\boldsymbol{q}-\boldsymbol{K}}^{0}$ - from a parabola, to being "deflected" by the $\varepsilon_{\boldsymbol{q}-\boldsymbol{K}}^{0}$ band and vice versa. As the bandstructure basically repeats itself such that every **K**/2 the plot is mirrored, if we include levels corresponding to more RLVs such as q$\pm$2K, q$\pm$K, and so on. Now, the black line can be indexed with n=1 while the red one with n=2. Including more RLVs introduces more bands, above the 2 bands plotted. All the unique solutions defining the band structure ε(**q**) lie in the region between $\pm\mathbf{K}/2$, which is what is referred to as the first Brillouin zone (1st BZ).

The bandgap of a crystal signifies the degree of near-degeneracy of solutions, i.e., how many energy eigenvalues are relatively close to each other around a given K-value, which is related to the strength of the potential ($2|U_{\boldsymbol{K}}|$) (i.e., the stronger the potential the more levels that will satisfy near degeneracy). This can be seen from another side; as "nature" does not accept the degeneracy of fermions (Pauli's exclusion principle), the solutions cannot be accessed, hence the energy region between a minimum of a band and the maximum of the previous band is referred to as the forbidden region. Therefore, the bandgap is a direct consequence of a periodic potential.

In the case of 3D periodic structures, beyond translation symmetry, one can rely on other symmetries defined by the structure to further reduce the BZ. However, it is still extremely complicated to calculate the complete band structure even for the case of weak periodic potential. However, one can still gain intuition from 1D models, like the Kronig-Penney model [30] and intuition gained from it [19], [31], [32].

Effective Mass

According to kaxiras we can define an effective mass through the second derivative of energy with respect to the wave vector [33]:

$$\frac{1}{\overleftrightarrow{m}_{ij}} = \frac{1}{\hbar^2}\frac{\partial^2 \mathcal{E}}{\partial k_i \partial k_j}, \tag{2.37}$$

for a given energy band n. The effective mass is generally expressed relative to its free-counterpart, i.e. the mass of an electron moving in vacuum, as in both cases they

can be expressed as propagating plane waves. Such quantity plays a major role in solid-state devices. However, the band structure problem, for real solids, becomes intractable in 3-D. Even though we can simplify the examined k-values through other symmetries, the problem arises from the potential term. Numerical methods have been developed to approximate the Hamiltonian to simulate real solids and generate their band structures for specific directions.

Within the band gap, there lies the FL, which is a statistical measure of how many states are occupied at a given temperature. At T=0, by definiton, all states below the FL are filled, exactly, while all states above it are unoccupied. The higher the temperature, the more states, above the FL, are filled. Bands above the FL are usually called conduction bands, as electrons lying there are able conduct electricity in the presence of an external electric field. There is one manner by which states above FL can be filled, momentarily, and this is through the reception of a photon with energy equivalent to the bandgap energy or higher. This is the main concept around which all optoelectronic devices revolve, including solar cells.

Due to the impossibility of generating analytical $\varepsilon - \boldsymbol{k}$ relations for 3D solids no matter how many symmetries it contains, density functional theory (DFT) was developed, where the Schrödinger equation for periodic structures with symmetries are solved self-consistently. One of the most successful methods used for generating band structures is referred to as the GW method, in term of predicting the bandgap energy of many solids. Thus one may rely on other generated features of the band structure, especially the curvature around band minima and maxima to extract the effective masses of charge carriers.

In real devices, a crystal is cut in planar form in a specific direction, such that when an external electric field is applied the electron is bound to move along the normal of the crystal. Thus, the band structure is reduced to a band diagram for the electron with an effective mass that includes correlation and/or exchange effects implicitly. If the effective mass is found experimentally, then it must include both correlationa and exchange effects. To find the best sectioning of a crystal, firstly, band diagrams

of single crystals are calculated numerically through DFT/GW calculations. For c-Si used in solar cell application, the <100> direction was found to be the most suitable.

Later, optimum combinations of interfaces are to be investigated. P. W. Peacock and J. Robertson have collected and calculated several band diagrams and structures showing conduction band minima (CBM) and valence band maxima (VBM) for several semiconductors and insulators in effort to guide the search for low carrier loss across heterojunctions [34], [35]. However, the barriers/offsets found numerically do not always correspond to real devices.

2.1.2 Modelling Surfaces

As crystals are not infinite in extent, some theories were developed for different types of crystals to describe their surfaces. The easiest surface to model would be the metallic surface. Classically, metals are known to forbid electric fields from propagating within them. In the presence of an electric field, the metallic surface will respond by developing a surface charge cancelling the propagation of electric fields inside. This view may not be generalized due to lack of almost-free electrons in other solids.

2.1.2.1 The WKB Approximation and Fowler-Nordheim Tunnelling (FNT)

The WKB approximation deals with non-trivial potentials experienced by quantum particles [36]. Following Sakurai, we start from the SE with an unspecified potential as:

$$\left(\frac{\hat{p}^2}{2m} + U(\boldsymbol{r}) - E\right)\psi = 0$$

$$\left(\frac{-\hbar^2}{2m}\frac{d^2}{d\boldsymbol{r^2}} + U(\boldsymbol{r}) - E\right)\psi = 0$$

(2.38)

Examining the 1D case $\boldsymbol{r} \rightarrow x$ and defining

$$k(x) \equiv \left[\frac{2m}{\hbar^2}\big(E - U(x)\big)\right]^{1/2}$$

(2.39)

As the quantity in parenthesis can be negative, we define

$$k(x) \equiv -i\kappa(x) \equiv -i\left[\frac{2m}{\hbar^2}(U(x) - E)\right]^{\frac{1}{2}} for\ E < V(x)$$

(2.40)

Then the SE becomes

$$\frac{d^2\psi}{dx^{\boldsymbol{2}}} + [k(x)]^2\psi = 0.$$

(2.41

For constant U, we get the plane-wave solutions, exp(±ikx). Assuming that U slowly varies with x, we try a solution in the form of a plane-wave whose wave-vector depends on position and has the form $W(x)/x\hbar$ such that the wavefunction becomes:

$$\psi = \exp\left({}^{iW(x)}/_{\hbar}\right).$$

(2.42)

Plugging this solution in the SE and evaluating:

$$\frac{d^2\exp\left({}^{iW(x)}/_{\hbar}\right)}{dx^{\boldsymbol{2}}} + [k(x)]^2\exp\left({}^{iW(x)}/_{\hbar}\right) = 0$$

$$\frac{d\left((i/\hbar)\frac{d(W(x))}{dx}\exp\left({}^{iW(x)}/_{\hbar}\right)\right)}{dx} + [k(x)]^2\exp\left({}^{iW(x)}/_{\hbar}\right) = 0$$

$$\left(\frac{i}{\hbar}\right)\frac{d\big(W(x)\big)}{dx}\frac{d\left(\exp\left({}^{iW(x)}/_{\hbar}\right)\right)}{dx} + (i/\hbar)\frac{d(W(x))}{dx}\exp\left({}^{iW(x)}/_{\hbar}\right) + [k(x)]^2\exp\left({}^{iW(x)}/_{\hbar}\right) = 0$$

$$\left(\frac{i}{\hbar}\right)^2 \frac{d\big(W(x)\big)}{dx}\frac{d\big(W(x)\big)}{dx}\exp\left({}^{iW(x)}/_{\hbar}\right) + (i/\hbar)\frac{d^2(W(x))}{dx^2}\exp\left({}^{iW(x)}/_{\hbar}\right) + [k(x)]^2\exp\left({}^{iW(x)}/_{\hbar}\right) = 0$$

$$\left(\frac{i}{\hbar}\right)^2 \left(\frac{d\big(W(x)\big)}{dx}\right)^2 + (i/\hbar)\frac{d^2(W(x))}{dx^2} + [k(x)]^2 = 0$$

$$-\left(\frac{d\big(W(x)\big)}{dx}\right)^2 + (i\hbar)\frac{d^2(W(x))}{dx^2} + \hbar^2[k(x)]^2 = 0$$

(2.43)

The concept of slow variation, within a region, can be understood by comparing the first and second derivative of the function:

$$\left|\frac{d\big(W(x)\big)}{dx}\right|^2 \gg \hbar\left|\frac{d^2(W(x))}{dx^2}\right|$$

(2.44)

Using this, we can approximate the SE to write the zeroth order approximation for $W(x)$:

$$\frac{dW_0(x)}{dx} = \pm\,\hbar k(x)$$

(2.45)

Then use it to find the first order approximation $W_1(x)$:

$$-\left(\frac{d\big(W_1(x)\big)}{dx}\right)^2 + (i\hbar)\frac{d^2(W_0(x))}{dx^2} + \hbar^2[k(x)]^2 = 0$$

$$\left(\frac{d\big(W_1(x)\big)}{dx}\right)^2 = \pm i\hbar^2\frac{d(k(x))}{dx} + \hbar^2[k(x)]^2 = 0$$

(2.46)

Such that

$$W(x) \approx W_1(x) = \pm\hbar\int^x dx'[k^2(x') \pm ik'(x')]^{1/2}$$

$$W(x) \approx W_1(x) = \pm\hbar \int^x dx'[k^2(x') \pm ik'(x')]^{1/2}$$

(2.47)

Given that $k'(x) \ll [k(x)]^2 (*)$, we can binomially expand the integrand

$$W_1(x) \approx \pm\hbar \int^x dx' k(x') \left[1 \pm \frac{ik'(x')}{2k^2(x')}\right]$$

$$W_1(x) \approx \hbar \left\{\frac{i}{2} \ln [k(x)] \pm \int^x dx' k(x')\right\}$$

(2.48)

Thus, we can express the wavefunction as

$$\psi \approx \exp\left({}^{iW_1(x)}/_{\hbar}\right) = \frac{1}{[k(x)]^{\frac{1}{2}}} exp\left[\pm i \int^x dx' k(x')\right].$$

(2.49)

We can check whether a potential is varying "slowly" enough from the first-order approximation. This relates the de Broglie wavelength of the particle to the variation of the potential [36].

However, one may not always need to approximate the SE. Such is the case for constant and linear potentials [37]. Consequently, Fowler and Nordheim solved the SE for a triangular barrier outside a cold metal exactly [20], which is almost never exactly the case at interfaces of interest. However, it proves useful to understand this barrier and in which cases it can arise, other than cold metal/vacuum interfaces. Ignoring image effects, for an electronic state above the FL, the potential takes the form:

$$U(x) = \begin{cases} \phi - qEx \; for \; x > 0 \\ 0 \; for \; x < 0 \end{cases}$$

(2.50)

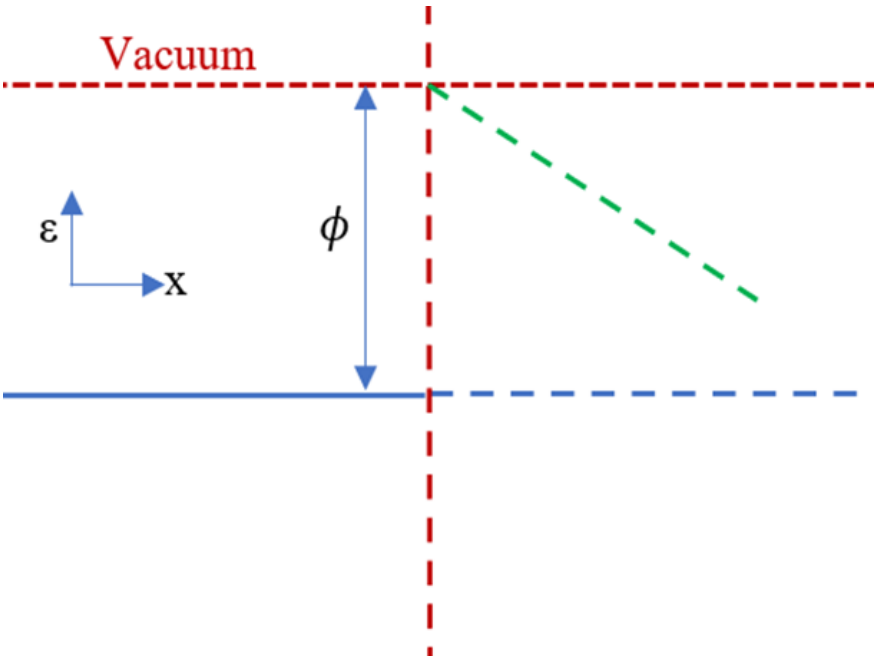

Figure 2.2 A schematic of the energy-space near the surface of a metal. On the left, the electron is bound to the metal but can freely move within it. Outside the metal under no electric field, the probability of finding an electron increases exponentially with distance, since it is practically a rectangular barrier, ignoring image effect. In the case of an external field, the classically forbidden region is reduced and hence the probability of finding an electron outside the metal is greatly enhanced.

where, ϕ is the barrier height, q is the fundamental charge of an electron, and E is the applied electric field component normal to the surface (Figure 2.2). The SE takes the form

$$H\psi = \begin{cases} \left(\frac{-\hbar^2}{2m}\psi'' + U(\boldsymbol{r})\psi\right) = \varepsilon\psi \; for \; x > 0 \\ \frac{-\hbar^2}{2m}\psi'' = \varepsilon\psi \qquad o.w. \end{cases}$$

(2.51)

With the definition

$$y = \left(x - \frac{(\phi - \varepsilon)}{F}\right)(2mF/\hbar)^{1/3}$$

(2.52)

The SE can be rewritten as

$$\frac{d^2\psi}{dy^2} + y\psi = 0$$

(2.53)

And the solution to the SE can be written in terms of Bessel functions of order 1/3:

$$\psi = \sqrt{y} J_{\pm 1/3}\left(\frac{2}{3} y^{3/2}\right)$$

(2.54)

Requiring a travelling wave far from the interface implies using Hankel functions of the second kind. After requiring the continuity of the wavefunction and its first derivative at the interface and some mathematical manipulation, the wavefunction coefficients, for both regions, can be found and an expression for the current of electrons exiting the metal under the external field is produced:

$$I = \frac{e}{\hbar}\frac{E^2}{\phi} exp\left(\frac{-4}{3\hbar}\sqrt{2m\phi^3}\Big/E\right)$$

(2.55)

2.1.2.2 Frenkel-Poole Emission (FPE) and Dielectric Surfaces

Frenkel described how, pre-breakdown, electrons in a dielectric responds to an electric field, explaining ionic conductivity thermodynamically [38]. In his paper, Frenkel describes crystals as a system of neutral atoms. For a given temperature, there will be ionized atoms where electrons will be "freely" swimming in the grid of neutral (polarizable) atoms and positive ions. As the fields of the positive ions are screened by the polarizable medium, the ionization energy will be reduced by a factor ε which is the dielectric constant of the medium. In an external field, the ionization energy is further reduced:

$$\Delta U = Er_0 + \frac{q}{4\pi\varepsilon r_0}$$

(2.56)

Where r_0 is given by $E = {e}/{4\pi\varepsilon {r_0}^2}$ such that

$$\Delta U = \sqrt{\frac{qE}{\pi\varepsilon}}$$

(2.57)

The ionic conductivity is assumed to be proportional to the number of free electrons due to the combined thermal ionization and field-assisted ionization:

$$\sigma = \sigma_0 \exp\left({\mathrm{q}\Delta U}/{kT}\right) \alpha \exp\left({-q(U_0 - \Delta U)}/{kT}\right)$$

(2.58)

In Frenkel's view of dielectric crystals, at T=0, the crystals are perfect in the sense there are no defects, and no atom is ionized, such that ionic conductivity is exactly zero. In this view, the proportionality becomes an equality.

2.1.2.3 Thermionic Emission (TE)

Although Schottky's model of the MS interface does not predict the right value for SBH, Bethe's theory of TE is still a powerful tool to characterize MS interfaces, where an effective barrier may be attributed to an interface constructed under certain parameters [2]. Starting with the main assumptions of the theory:

- The barrier is much greater than the thermal voltage: $q\phi_B \gg kT$
- Thermal equilibrium is established.
- Existence of a net current does not affect the equilibrium.
- Ignore the image effect.

And the postulate that conduction electrons' energy is purely kinetic. Now, we may state that the total current density is equal to the current density of electrons going from semiconductor to metal ($J_{s\to m}$) minus the current density going from metal to semiconductor ($J_{m\to s}$):

$$J_{tot} = J_{s\to m} - J_{m\to s}\,.$$

(2.59)

From the semiconductor's side, the current density is equal to the number of electrons whose energies are enough to overcome the barrier moving towards the interface with velocities corresponding to their energies:

$$J_{s\to m} = \int_{\varepsilon_F + q\phi_B}^{\infty} q v_x dn,$$

(2.60)

where

$$dn = N(\varepsilon)F(\varepsilon)d\varepsilon = \frac{4\pi(2m^*)^{3/2}}{h^3}(\varepsilon - \varepsilon_C)^{1/2} exp\left({}^{-(\varepsilon - \varepsilon_C + qV_n)}/_{kT}\right) d\varepsilon$$

(2.61)

and

$$qV_n = \varepsilon_C - \varepsilon_F.$$

(2.62)

Using the postulate:

$$\varepsilon - \varepsilon_C = \frac{1}{2}m^* v^2$$

$$(\varepsilon - \varepsilon_C)^{1/2} = \left(\frac{m^*}{2}\right)^{1/2} v \;\; and \;\; d\varepsilon = m^* v dv$$

(2.63)

Such that

$$dn = \frac{4\pi(2m^*)^{3/2}}{h^3}\left(\frac{m^*}{2}\right)^{1/2} v \;\; exp\left({}^{-qV_n}/_{kT}\right) exp\left({}^{-m^* v^2}/_{2kT}\right) m^* v dv$$

$$dn = 2\left(\frac{m^*}{h}\right)^3 \; exp\left(-qV_n/kT\right) exp\left(-m^*v^2/2kT\right) 4\pi v^2 dv$$

(2.64)

Which is the number of electrons per unit volume that have speeds between v and $v + dv$ distributed over all directions. Expanding v:

$$v^2 = v_x^2 + v_y^2 + v_z^2$$

$$4\pi v^2 dv = dv_x dv_y dv_z$$

(2.65)

The current $J_{s\to m}$ takes the form:

$$J_{s\to m} = \int_{\varepsilon_F + q\phi_B}^{\infty} qv_x 2\left(\frac{m^*}{h}\right)^3 \; exp\left(-qV_n/kT\right) exp\left(-m^*v^2/2kT\right) dv_x dv_y dv_z$$

$$= 2q\left(\frac{m^*}{h}\right)^3 e^{-qV_n/kT} \int_{\varepsilon_F + q\phi_B}^{\infty} v_x \; exp\left(-m^*\left(v_x^2 + v_y^2 + v_z^2\right)/2kT\right) dv_x dv_y dv_z$$

$$= 2q\left(\frac{m^*}{h}\right)^3 e^{-qV_n/kT} \int_{v_{0x}}^{\infty} v_x \; e^{-m^*v_x^2/2kT} dv_x \int_{-\infty}^{\infty} e^{-m^*v_y^2/2kT} dv_y \int_{-\infty}^{\infty} e^{-m^*v_z^2/2kT} dv_z$$

(2.66)

where

$$v_{0x} = 2q\,(V_{bi} - V)/m^*$$

(2.67)

And V is the applied potential across the barrier. The integrals in the y and z directions are in the form of the Gaussian integral $\int_{-\infty}^{\infty} e^{-ax^2} dx$ with $a = \frac{-m^*}{2kT}$. Therefore,

$$J_{s\to m} = 2q\left(\frac{m^*}{h}\right)^3 e^{-qV_n/kT}\frac{2kT}{m^*}\pi \int_{v_{0x}}^{\infty} v_x \; e^{-m^* v_x^2/2kT} dv_x$$

(2.68)

Solving the last integral by substitution ($v_x^2 = u,\ 2v_x dv_x = du$):

$$\int_{v_{0x}}^{\infty} v_x \; e^{-m^* v_x^2/2kT} dv_x = \frac{1}{2}\int_{u=v_{0x}^2}^{\infty} e^{-m^* u/2kT} du$$

$$= \frac{-kT}{m^*} exp\left(\frac{-m^* v^2}{2kT}\right)\Bigg|_{v_{0x}}^{\infty}$$

$$= \frac{kT}{m^*} exp\left(\frac{-m^* v_{0x}^2}{2kT}\right)$$

(2.69)

Therefore, the current density from the semiconductor's side is

$$J_{s\to m} = 2q\left(\frac{m^*}{h}\right)^3 e^{-qV_n/kT}\frac{2kT}{m^*}\pi\frac{kT}{m^*} exp\left(\frac{-m^* v_{0x}^2}{2kT}\right)$$

$$J_{s\to m} = \frac{4\pi m^* q(kT)^2}{h^3} exp\left(-qV_n/kT\right) exp\left(\frac{-m^* v_{0x}^2}{2kT}\right)$$

(2.70)

Where $\frac{4\pi m^* q k^2}{h^3} = A^*$ is defined as Richardson's constant. Finally, we express V_n and v_{0x} in terms of the band diagram quantities and using $q\phi_B = V_{bi} + V_n$, we reach the expression:

$$J_{s\to m} = A^* T^2 exp\left(-qV_n/kT\right) exp\left(\frac{-q(V_{bi} - V)}{kT}\right)$$

$$= A^* T^2 exp\left(\frac{-q(V_{bi} + V_n - V)}{kT}\right)$$

$$J_{s\to m} = A^{*}T^{2}exp\left(^{-q\phi_B}/_{kT}\right)exp\left(\frac{qV}{kT}\right)$$

(2.71)

As for the current density from the metal's side, since the FL of metals does not change depending on the applied voltage, electrons going from $m \to s$ will always see the same barrier. Therefore,

$$J_{m\to s} = A^{*}T^{2}exp\left(^{-q\phi_B}/_{kT}\right)$$

(2.72)

Therefore, the TE current density is:

$$J_{TE} = J_{s\to m} - J_{m\to s}$$

$$J_{TE} = \left[A^{*}T^{2}exp\left(^{-q\phi_B}/_{kT}\right)\right]\left(exp\left(\frac{qV}{kT}\right) - 1\right)$$

(2.73)

Where the quantity inside the square brackets is referred to as the saturation current, J_{sat}. However, in real contacts, the current does not really saturate. This is due to the image effect, which was neglected in the derivation. It is usually partially accounted for by n the ideality factor such that:

$$J_{TE} = J_{sat}\left(exp\left(\frac{qV}{nkT}\right) - 1\right)$$

(2.74)

Including the diffusion current can be summarized as an adjustment in the Richardson constant [2]. For n-type Si <100>, $A^{*} \cong 120\ A.K^{-2}.cm^{-2}$ while for p-type Si; $A^{*} \cong 30\ A.K^{-2}.cm^{-2}$ in the typical electric field range, since it is electric field dependent. Such specifications contribute to the obscurity of MS barrier height reports, albeit not by much; $\sim 20\ meV$ for the use of different values for the effective mass in Richardson's constant.

2.1.2.4 The image effect

The image effect could be thought of as one of the manners with which the discontinuity of matter is smoothed in space as potential fields cannot be discontinuous, except in electrostatics or other theoretics. The barrier ($q\phi_B = V_{bi} + V_n$) used in the previous section is necessarily the reduced barrier due to the image effect. Since the image-effect is dependent on the applied field, the barrier reduction is, likewise, field dependent. The dependence on the applied field may be accounted for by the ad-hoc ideality factor, n. Modelling the current as such will yield an effectively lowered barrier [2] which is the same case for FNT [21], [37], [39]. In the reverse bias, the current's dependence on the barrier-lowering is much stronger than in the forward bias regime [2]. Thus, the explicit inclusion of the image-effect in the analysis is a must for a full characterization of the interface [40].

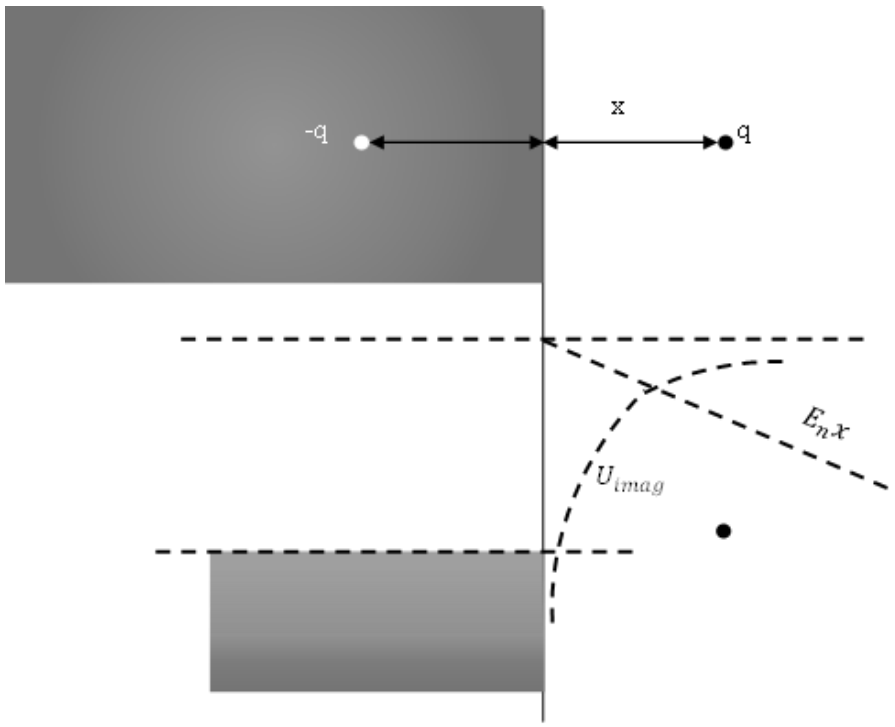

Figure 2.3 Schematics of the image effect in the case of a metallic surface along with a band diagram representation of the same configuration where E_n is the electric field component normal to the surface.

The simplest case of the image effect is the electrostatic configuration where there is a metallic surface with an electron, q, being placed in front of it at distance x, normal to the surface (Figure 2.3). Due to the property of metals of not allowing electric fields to develop within them, the potential field is necessarily zero (or a constant) below the surface [3]. The electric field outside the metal will, then, behave as if there is an oppositely charged particle (hole) within the metal that *seems* to be located at the same distance from the surface. This manifests as a surface charge on the metal (that negate the electric field) since the image-particle is a fictitious one. Hence, the force that the charged particle experiences is an attractive one, towards the surface. The potential due to the image-particle at distance x from the surface:

$$U_{imag} = \frac{q}{16\pi\varepsilon_0}\frac{1}{x} \tag{2.75}$$

In the presence of an electric field, the potential becomes:

$$U = \frac{q}{16\pi\varepsilon_0}\frac{1}{x} + E_n x \tag{2.76}$$

Where x is the distance between the metal and the electric field source. The amount by which the barrier has been lowered can be found by taking the first derivative of the potential and setting it to zero:

$$\frac{dU}{dx} = E_n - \frac{q}{16\pi\varepsilon_0}\frac{1}{x^2} = 0 \tag{2.77}$$

$$x_m = \sqrt{\frac{q}{16\pi\varepsilon_0 E_n}} \tag{2.78}$$

Where x_m corresponds to the place where the potential barrier is at its peak. Plugging it in the expression for the potential:

$$U(x_m) = \Delta\phi = \frac{q}{16\pi\varepsilon_0}\frac{1}{x_m} + E_n x_m$$

$$U(x_m) = \sqrt{\frac{qE_n}{16\pi\varepsilon_0}} + E_n\sqrt{\frac{q}{16\pi\varepsilon_0 E_n}} = \sqrt{\frac{qE_n}{4\pi\varepsilon_0}}$$

$$\Delta\phi = \sqrt{\frac{qE_n}{4\pi\varepsilon_0}}$$

(2.79)

Where $\Delta\phi$ is the barrier reduction. Recalling the FNT barrier, which was a constant term plus a term linear in E. If we add this barrier lowering term to the problem, we will need to use the WKB approximation to find an expression for the current.

In the case of a metal/vacuum interface, the expression for E is simply the applied voltage divided by the distance between the metal and electrode. On the other hand, in the case of a MS interface, the expression for E is not as simple. However, simplifying the interface by approximating it as an abrupt p++/n junction, we can find the electric field across the junction through Poisson's equation [41].

2.2 Literature Review

After establishing the potentially relevant theories regarding bulk properties and surface modelling, we examine the observations done in the literature over the last 8 decades. Due to the huge time span of research into semiconductors, some of the observed phenomena was due to the primitive manufacturing procedures of devices. Such observations were disregarded.

2.2.1 MS Interfaces

Almost all MS contacts did not strictly follow Schottky's rule and in the case of Si and germanium (Ge), the SBH became almost metal independent. Bardeen [18]

proposed that the reason is due to the presence of states in the bandgap that are created due to lattice termination. Such states could be collectively thought of as an energy level (termed as charge neutrality level (CNL)). If the Fermi level (FL) is above CNL, it would mean that the surface is negatively charged, and vice versa, this concept was developed by Tersoff [19]. This forces the FL to be pinned near the CNL to achieve charge neutrality with the bulk, before contact.

Cowley and Sze introduced the S-Parameter [22], a quantification of how strongly an interface obeys the Schottky-Mott rule:

$$S = \frac{\partial \phi_B}{\partial \phi_M} \tag{2.80}$$

This establishes a FLP scale where S = 1 corresponds to the Schottky-Mott rule (the Schottky limit (SL)) and S = 0 corresponds to complete pinning (the Bardeen limit (BL)). Simultaneously, Heine [23] proposed a semi-quantitative analysis of the surface states. He postulated that k-matching electronic wave functions with energies around the mid-gap are responsible for the FLP observed, which were later referred to as MIGS. This is further corroborated by the observed transition from almost complete pinning in the cases of elemental semiconductors (Si and Ge) to a weakened pinning observed in the silicides and germanides, which generally have a lower electronic density of states than pure metals [42]–[44]. Going along the MIGS analysis, one finds a simple guideline: *decrease the metal's electronic density at the contact to decrease the pinning effect*. This is what Nishimura et al. [45] did by studying the Bismuth (Bi)/Si and Bi/Ge interfaces and found that Bi obeys the Schottky-Mott rule. This was attributed to the Bi low carrier density ($\sim 10^{17}\ cm^{-3}$) even though its work function has a comparable work function to that of aluminum (Al: 4.16-4.3 eV; Bi: 4.26 eV). Thus, it is proven, experimentally, that the density of conducting electrons on the metal side contributes to the pinning. In the same work, they experimented the surface orientation effect from the semiconductor side where they revealed some dependence. This is understandable since the orientation dictates

the surface density of atoms and hence electronic states [46]. Such effect was obscured by the pinning.

C.A. Mead measured the barrier height of CdS_xSe_{1-x} contacted with different metals (e.g., Cu, Ag, Au, Pt) [47]. A transition from a metal dependent barrier height for pure cadmium sulfide (CdS), corresponding to the SL, to an almost independent barrier height for pure cadmium selenide (CdSe), corresponding to the BL. This transition is attributed to the high *ionicity* of CdS compared to CdSe, based on Shockley's description of surface states in non-metals [48]. Inspired by Mead's experiment, Kurtin et al. [49] tried to establish the relation between the S-Parameter with the degree of ionicity and quantified ionicity using Pauling's electronegativity scale [50] Catlow et al. [51] and J. Robertson [35] have attempted to point out the inconsistencies accompanying the definition of ionicity and its ability to predict the SBH, respectively. Later, J. Robertson [35], assessed the relation between the extracted S-Parameter for various crystals as a function of polarizability/static dielectric constant, and Miedema's electronegativity scale [52] and found an undeniable trend. All these observations bring us to conclude that the surface states are controlled by the electrons wave-function with the unit cell of crystals.

In this context, J. C. Phillips [53] and C. Falter et al. [54] defined ionicity by examining the orbital wavefunction of valence electrons (sp^3 hybridization) and charge transfer between the constituent ions of different crystals, respectively. Interestingly, J. C. Phillips' definition coincides well with the polarizability/permittivity relation shown by J. Robertson [35]. The ionicity analysis done by J. C. Phillips shows that CdS and CdSe are somewhat ionic. This is due to the exclusion of d-electrons from J. C. Phillips analysis. Additionally, J. Tersoff [19] calculated the CNL of the surface semiconductors where he considered the creation of a dipole, which is associated with the gap states, generated by lattice termination. His values for CNL corresponded very well with where the FLP occurred in Ge and Si in other reports [55].

2.2.2 Surfaces and Interfaces

However, the interface subtleties remain hidden, especially if it is composed of several layers. To reveal such subtleties, it is easier to start with the observed behavior of simple junctions such as Metal-Insulator (MI), MS, and Semiconductor-Insulator (SI). Starting with the Metal/Vacuum interface, the only transport mechanism would be Fowler-Nordheim Tunneling (FNT) as there are no states to be occupied in vacuum.

By considering this, the set of experiments done by C. K. Perkin et al. [56] elegantly demonstrate the transition from defect/trap assisted transport to pure FNT in terms of increasing degrees of purity and order of the solution based deposited Al_2O_x on a TaN substrate. Having prepared the flat-Al_{13} precursor solution, the conversion to Al_2O_x occurs by annealing the substrate after spin-coating. In the first experiment, they controlled the purity of Al_2O_x by varying annealing temperatures and monitoring the presence of H_2O and NO. For nominally 9 nm thick Al_2O_x capped with Al, the current density as a function of electric field curves shows the transition from Frenkel-Poole (FP) emission (T_{Anneal} = 350 C°) to pure FNT (T_{Anneal} = 600 C°), as different species desorb at different temperatures, which acted as defects. In the second experiment, they controlled the purity of the precursor, such that, metal impurity is varied. Again, a transition from space-charge-limited conduction (SCLC) towards FNT was observed as metal impurities are diminished. This could be used to view insulators, in the nanoscopic regime, as an "*effective*" vacuum from the electrons' perspective.

Furthermore, several I-VII and II-VI crystals (ionic crystals) were studied spectroscopically under different deposition conditions. It was a common observation to find epitaxial growth with minimal mismatch with the substrates [57]–[60]. Combining XPS and UPS to study the deposition process in-situ effectively reveals the actual band diagram. Using UPS, one could measure the FL/work function at the surface of a material. It was also common observation that depositing

ionic crystals lowered the UPS measured work function of the surface [5], [14], [58], [61]–[64].

For the case of MI interfaces, metals did not show any chemical reaction with the ionic crystals. However, while R. Schlaf et al. [63] were investigating LiF_x deposited on Al and Pt, they observed a shoulder in the Al *2p* signal, which is indicative of oxidation of Al and was attributed to the water that chemisorbed upon depositing 1Å of LiF_x. In the same work, the thickness dependent work function of both interfaces was also measured and found that for Al/(3 nm) LiF_x a work function of 2.5 eV and practically saturating at this value upon further increasing the LiF_x thickness deposition. As for the Pt/LiF_x interface, at 3 nm coverage the work function was found to be 3.8 eV, with no saturation observed in the measured range of depositing 25 nm LiF. The work function seemed to be decreasing linearly for the Pt/LiF_x interface.

Additionally, Y. M. Wang et al. [64] deposited LiF_x on Diamond with different surface properties (H- and O- terminated) where they found that the effective work function ϕ_{eff} of LiF_x saturates at ~2.5 eV after 2.5 nm thickness. Zhengyi Sun et al. [26] further investigated the interface of LiF_x with coinage metals where they found after deposition of 3 nm of LiF_x on any of the considered metals (Cu, Ag, and Au), the ϕ_{eff} is ~3.8 eV. Similarly, rubidium fluoride was also shown to lower the work function of polycrystalline diamond [62].

In another work [57], CaF_2 and SrF_2 were deposited onto InP substrates using molecular beam epitaxy (MBE), at substrate temperature of 820 K, and similarly showed crystalline growth and lack of chemical reaction at the interface was confirmed. The (Ca/Sr)F_2 bands were found to bend at the interface and lower the work function of the substrate from 4.1 to 2.7 eV for InP/CaF_2 and 2.4 eV for InP/SrF_2. Due to the chemical inertness of the interfaces and continuation of bending beyond the screening of the substrate, it was concluded that Frenkel defect pairs were responsible for the observed bending. In bulk, the defects are created in pairs to maintain crystal neutrality, while at the surface one type of defect is more

thermodynamically favorable than the other which creates a potential difference between surface and bulk [65]. Modelling the defect pair density as a step function and using independently found values of enthalpy/entropy of Frenkel defect pair formation, the bulk defect pair density was found to correspond to the substrate temperature at which deposition occurred, not room temperature at which measurements were collected. Unfortunately values of enthalpy/entropy of formation of defects are dissimilar in different sources, and in the case of entropy of formation information is wanting, such that one cannot specify the concentration of defects of such crystals, with certainty, to predict which would work better as ILs for c-Si [66]–[69].

The work function discrepancy

Since the discovery of the photoelectric effect, measurements of metal work function started to be complied. One might expect that due to the fact that the photoelectric phenomenon is a threshold phenomenon, the error in extracting the work function of metal surfaces would not be large and should be around the thermal voltage ($\sim 26\ meV$). However, a glance at literature tells us otherwise. R. Smoluchowski was one of the first to describe how one material can possess multiple work function values, due to the fact that at different lattice orientation the electron perceives different atomic densities [70]. Taking the surface of Au as an example. In the case of thermal evaporation, we expect amorphous deposition. Interestingly, single crystalline and polycrystalline clusters were observed in the same deposition [71]. This is an example of how it is difficult for any exact prediction to be made regarding interfaces, although reproducible.

CHAPTER 3

INSTRUMENTS AND MEASURING TECHNIQUES

In this chapter, we discuss the tools used to construct the devices on which we experimented, and the tools/analyses used to characterize said devices. The Si wafers used in this study were purchased and later characterized by us for crystallinity and resistivity values. All Si wafers used for characterization were RCA/RCA2 cleaned and dipped in diluted HF (to remove the native oxide) immediately before depositions.

3.1 Deposition Techniques

There are several techniques of depositing one solid onto another solid. The manner in which this was done changed since the time of Schottky. This may add insight as to why there were differences in reported values of the Schottky barrier height over the decades.

3.1.1 Physical Vapor Deposition (PVD)

There are multiple ways in which thin layers are deposited onto a substrate. In this thesis, thermal evaporation is used, exclusively. In thermal evaporation, the main idea is that solids are placed in conductive boats inside a vacuum chamber where pressure can go as low as $1x10^{-7}$ Torr (i.e., 1 trillionth the number of atoms in normal atmosphere is present in the vacuum chamber) such that once they become liquid they easily and controllably evaporate then adsorb to the substrate. Then, using a sensor based on a quartz crystal, the amount of material evaporated is monitored in

terms of thickness with angstrom resolution after selecting the parameters identifying the material (Z-ratio and density) [72].

3.2 Characterization Techniques

For our study of ultrathin ILs, we require high accuracy in knowing the deposited thicknesses and crystallinity such that we can quantify the electrical properties of such layers with certainty.

3.2.1 Spectroscopic Ellipsometry

As we are dealing with ultrathin layers, we must cross check the accuracy of the quartz thickness monitor, in the vacuum chamber. The thickness monitor is set up with a tilt, slightly far from the sample holder. This causes it to be at the edge of the "vapor" and hence will not report the exact thickness of deposition. Using spectroscopic ellipsometry, one can measure thicknesses with a resolution of few angstroms. Thus, basic knowledge on how it operates is integral to the process of quantifying the effects that the ILs have in the MIS geometry.

The basic principle of spectroscopic ellipsometry is using linearly polarized light to investigate the properties of thin films by analyzing the reflected/transmitted light. Since the sample's thickness, refractive index, and extinction coefficient uniquely alter the incident electromagnetic wave (light), for a given incident angle and wavelength. Upon irradiating the sample with linearly polarized light the reflected light becomes elliptically polarized, almost always, hence the name of the technique. The reflected light is compared to the incident one in terms of phase difference (Δ) and the amplitude ratio (ψ) of (p)arallel-polarized light and (s)urface-polarized light. The measurement sensitivity is maximized when the incident light is at the Brewster angle dictated by the sample, where the ratio between p-polarized light and s-polarized light is maximized. Since we are dealing with c-Si, the incidence angle should be around 73° [73].

Upon retrieving ψ and Δ, we can find the refractive index (n) from ψ and the extinction coefficient (k) from Δ using the Fresnel equations defining the reflection coefficients; the ratio of reflected s-polarized (r_s) and p-polarized (r_p) light to the incident light (r_p is essentially the same):

$$r_s \equiv \frac{E_r}{E_0} = \frac{ncos\theta - n'cos\theta'}{ncos\theta + n'cos\theta'}$$

(3.1)

Where n is simply 1 for air and n' is that of the sample, θ and θ' are incident angle and transmittance angle, respectively, and E_0 is the incident electric field component (s- or p-polarized).

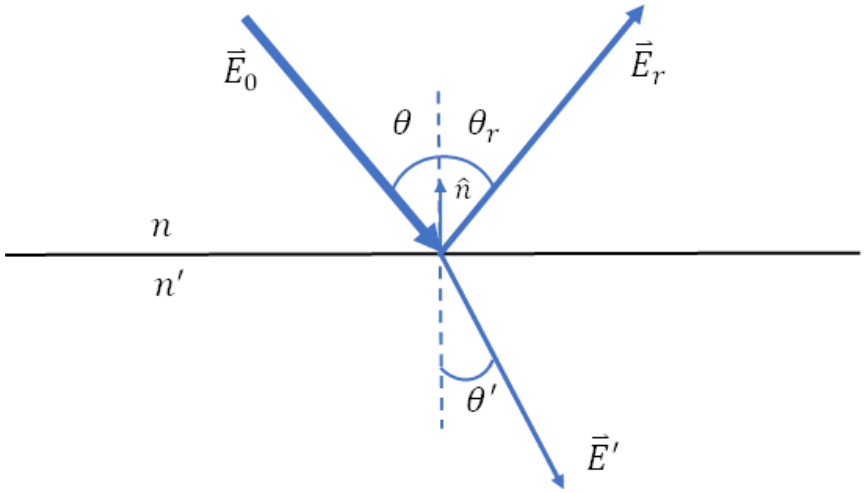

Figure 3.1 Electric field components at the boundary defined by a discontinuity in the refractive index.

Equation (3.1) can be derived by imposing the appropriate boundary conditions on the electric field components. From the definition of the electric and magnetic fields, the tangential components ($E_\parallel$ and $H_\parallel$) and the normal component ($D_\perp$ and $B_\perp$) are continuous, such that the boundary conditions at the interface are [3]:

$$\left[\left(\overrightarrow{E_0} + \overrightarrow{E_r}\right) - \overrightarrow{E_0'}\right] \times \hat{n} = 0\,, (E_\parallel\, cont.)$$

(3.2)

$$\left[\varepsilon\left(\overrightarrow{E_0}+\overrightarrow{E_r}\right)-\varepsilon'\overrightarrow{E_0'}\right].\hat{n}=0\,,(D_\perp\ \text{cont.})$$

(3.3)

$$\left[\frac{1}{\mu}\left(\vec{k}\times\overrightarrow{E_0}+\overrightarrow{k_r}\times\overrightarrow{E_r}\right)-\frac{1}{\mu'}\overrightarrow{k'}\times\overrightarrow{E_0'}\right]\times\hat{n}=0\,,(H_\parallel\ \text{cont.})$$

(3.4)

$$\left(\vec{k}\times\overrightarrow{E_0}+\overrightarrow{k_r}\times\overrightarrow{E_r}-\overrightarrow{k'}\times\overrightarrow{E_0'}\right).\hat{n}=0\,,(B_\perp\ \text{cont.})$$

(3.5)

Where $\hat{n}$ is a unit vector normal to the surface. First, we consider when the electric field component is perpendicular to the plane of incidence (defined by the wavevector $\vec{k}$ and $\hat{n}$, and labelled s-polarized). Along with the reasonable approximation that the relative permeabilities of air and our layers are 1, it can be shown that the ratio between the reflected and incident is (3.1). Using conditions (3.2) and (3.4):

$$E_0+E_r-E_0'=0$$

(3.6)

$$\sqrt{\frac{\varepsilon}{\mu}}(E_0-E_0'')cos\theta-\sqrt{\frac{\varepsilon'}{\mu'}}E_0'cos\theta'=0$$

(3.7)

Such that,

$$\sqrt{\frac{\varepsilon}{\mu}}(E_0-E_r)cos\theta-\sqrt{\frac{\varepsilon}{\mu}}(E_0+E_r)cos\theta'=0$$

$$E_0=E_r\frac{\sqrt{\varepsilon_0\mu_0}\left(\frac{n}{\mu}cos\theta-\frac{n'}{\mu'}cos\theta'\right)}{\sqrt{\varepsilon_0\mu_0}\left(\frac{n}{\mu}cos\theta+\frac{n'}{\mu'}cos\theta'\right)}\cong E_r\frac{(ncos\theta-n'cos\theta')}{(ncos\theta+n'cos\theta')}$$

(3.8)

For the p-polarized component, we use the other two boundary conditions and find that the refractive indices are interchanged in equation (3.1) (i.e., n takes the place of n' and vice versa). Next, we can compute (n, k) through the definition (in the reflection regime):

$$\rho \equiv \tan(\psi) e^{i\Delta} \equiv \frac{r_s}{r_p} \tag{3.9}$$

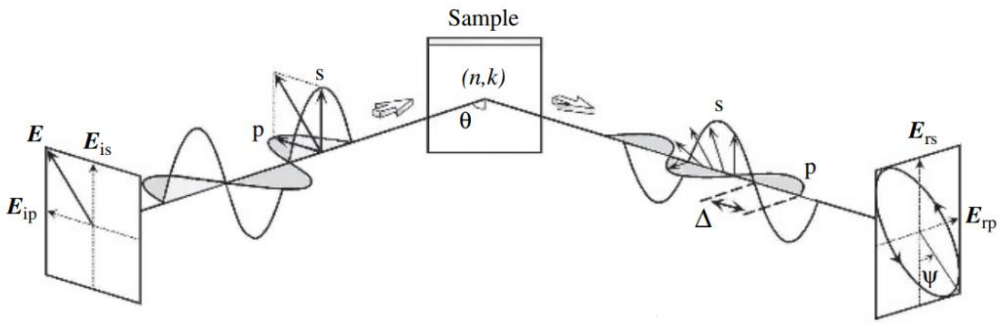

Figure 3.2 Schematic of incident linearly polarized light and reflected elliptically polarized light. Retrieved from [73].

The equations for the reflection coefficients (r_s and r_p) are slightly different when analyzing a thin layer on top of a substrate, where the transmitted light from the layer of interest reflects at the boundary (between it and that of the substrate) and contributes to the measured reflected light, with a phase difference. This phase difference is how we can measure the thickness of the thin film. Coupling our knowledge of the substrate's complex refractive index with the measured (ψ and Δ), we can determine the thickness of the ultrathin layer [73].

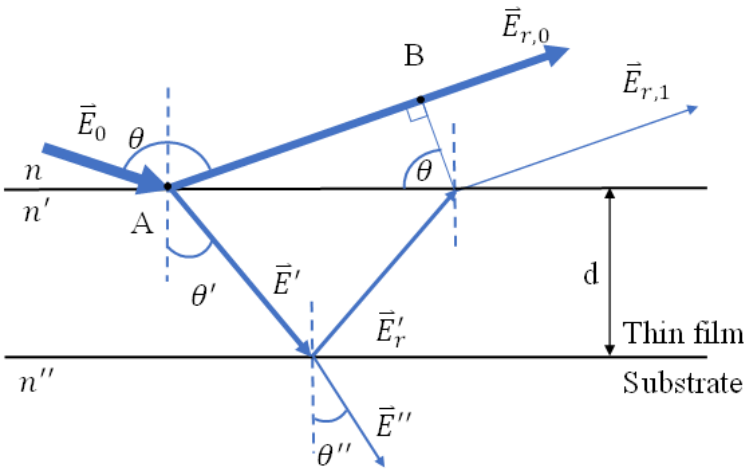

Figure 3.3 Electric field components of the primary and secondary beam when considering thin film interference.

In Figure 3.3, we see the primary reflected beam ($\vec{E}_{r,0}$) and the secondary one ($\vec{E}_{r,1}$). From the figure, for a given wavelength λ, the optical path difference between the primary beam and the secondary one amounts to:

$$\alpha = \frac{4\pi d n'}{\lambda} cos\theta'$$

(3.10)

Which introduces a phase difference ($e^{-i\alpha}$) that either causes constructive or destructive interference with the primary beam. With each successive reflection from the thin film/substrate interface, higher order reflections diminish while picking up cascaded phase difference. Thus, including the contribution of all reflections coming from the thin film/substrate interface, the total reflected ratio is [73]:

$$r = \frac{E_{r,0} + E'_r e^{-i\alpha}}{1 + E_{r,0} E'_r e^{-i\alpha}}$$

(3.11)

Where $E_{r,0}$ is that of the previous analysis (E_r), and

$$\vec{E}'_r = \frac{n' cos\theta' - n'' cos\theta''}{n' cos\theta' + n'' cos\theta''}$$

(3.12)

For s-polarized light. Again, the refractive indices are interchanged for p-polarized light. Since the substrate is Si and its extinction coefficient is nonzero in the range of analysis ($1.23 - 4.29\ eV$), the complex nature of the refractive index must be used in the expressions.

As an example, we show the results of the analysis of one of our layers (NaF) under study (Figure 3.4). We have deposited 250 Å of NaF on a clean Si substrate, according to the quartz sensor. The analysis (angle of incidence$= 70°$) shows that approximately 272 Å were deposited. Another deposition (not shown) was done for reproducibility, where the layer was found to be 258 Å. Taking the average, the results tell us that for every angstrom claimed (by the sensor) to be deposited, 1.06 Å is actually deposited. The refractive index found in the analysis matched that of literature, almost exactly (difference ~ 0.005 at $\lambda = 632\ nm$) [74][75]. This difference could be due to a combination of the relaxation at the interface and the error in the measurements in the literature values (± 0.008) [75]. However, it is too small for any conclusions to be made, other than that we have NaF.

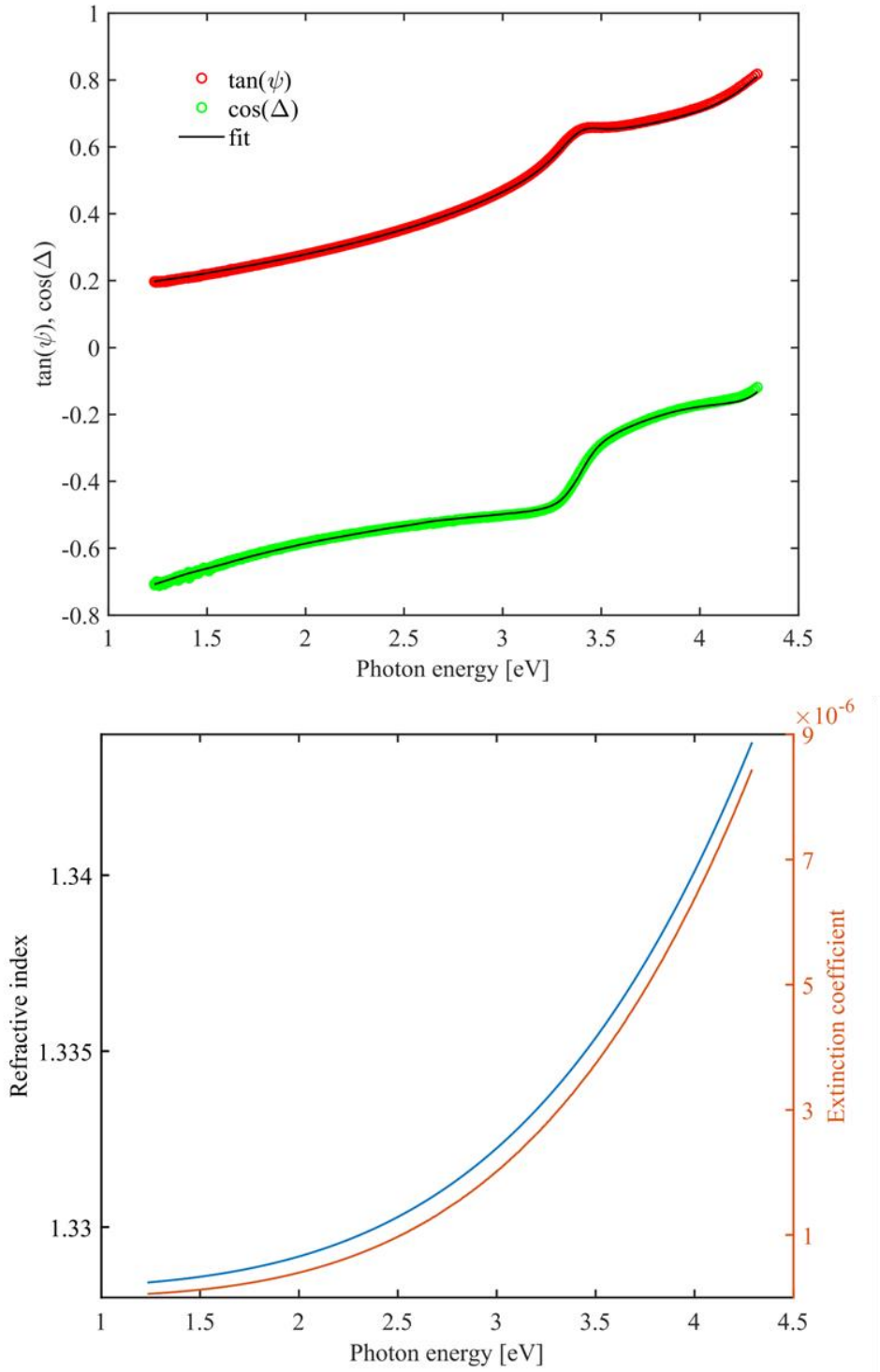

Figure 3.4 In the upper graph, we have the measured values of psi and delta along with their fit using the Caushy model. Using these values along with the expected contribution from the Si substrate, the refractive index and extinction coefficent of our thin film is found.

3.2.2 X-Ray Diffraction (XRD)

Returning to the concept of XRD, we recall how Bragg observed unique X-ray reflection patterns from macroscopically crystalline solids. His formulation led to the characterization crystallinity of solids; from how many orientations there are in a poly-crystalline solid to the lattice constant of powders. W.L. Bragg considered the crystal as composed of evenly spaced parallel planes of ions where reflection peaks occur at the same angle of incidence (specular reflection) when the reflected ray constructively interfere with a reflected ray from the adjacent plane. The angle at which this peak occurs corresponds to the wavelength of the incident ray and the spacing between crystal planes. The condition for constructive interference is that the path difference of the rays is an integer multiple of the wavelength. Thus, for a given set of planes separated by distance d, the "Bragg" condition is:

$$n\lambda = 2dsin\theta \tag{3.13}$$

Where θ is the incident angle which is conventionally measured from the surface plane as opposed to the normal plane in optics (previous section). Another physicist, Von Laue, similarly formulated the diffraction of X-rays, by considering the crystal to be composed of evenly spaced ions in a Bravais lattice. His conclusion was the same, minus the assumption of specular reflection [17]. Thus, scanning for the angle at which reflection peaks occur will provide us with the interatomic spacing. Learning the interatomic spacing from known samples allows us to identify layers and their crystal orientations.

3.2.3 Dark Current-Voltage (I-V)

Extracting electronic properties from semiconductor-based devices is somewhat challenging. This is why, several methods exist for extracting, contact resistance and barrier heights. We chose to use Cheung's analysis and the Cox-Strack method (CSM) to find the barrier heights and contact resistivity, respectively.

3.2.3.1 CSM

A well-known method for extracting contact resistivity is the CSM. This method is based on constructing different contacts surface different areas on the same substrate such that one is able to isolate the contact term in the total resistance. The total resistance is assumed to be a combination of 3 resistors connected in series. Thus, the total resistance can be expressed as such:

$$R_T = R_C + R_S + R_0$$

(3.14)

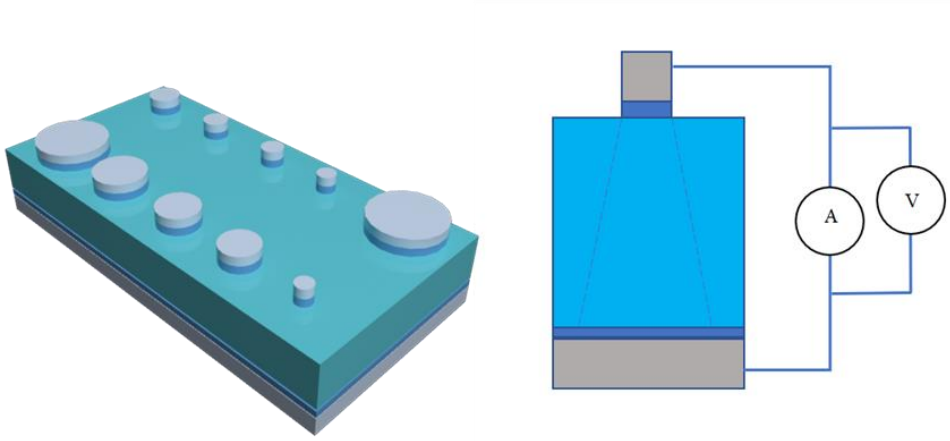

Figure 3.5 On the left we have a substrate with differently sized contacts on the top and on the bottom, there is an ohmic contact (drawn by my friend, Loay Akmal). On the right we have the electrical schematic of the device. The electric field is found to spread throughout the substrate in a conic-like fashion. The lower contact must be ohmic such that its resistance is not current dependent.

Where R_S is the spreading resistance of the substrate, which was based empirically on electrolytic tank measurements [76]:

$$R_S = \frac{\rho}{\pi d} arctan \frac{4t}{d}$$

(3.15)

$$R_C = \frac{\rho_C}{\pi d^2/4} = \frac{\rho_C}{Area}$$

(3.16)

and R_0 is the residual resistance which is composed of the resistance of that which is neither contact nor substrate. This quantity (R_0) is assumed to be contact and substrate independent and to be constant. The method was first devised for ohmic devices such that R_T could be extracted from the linear I-V measurement. On the other hand, for rectifying contacts R_T would be hard to extract. Some researchers [77] would take a linear regression of the I-V curve at several voltages to approximate R_T. However, there is a more methodological manner by which we can extract R_T, which is using Cheung's analysis. This was dubbed "Expanded CSM" [78]. In Cheung's analysis, the resistance is found by taking the derivative of the potential with respect to the natural logarithm of the current and extracting the slope. Starting from the diode equation:

$$I = I_s \left[\exp\left({\beta(V - IR)}/{n}\right) - 1\right], \beta = q/k_B T \tag{3.17}$$

When we are looking at forward bias of $V \geq 3kT/q$, we may approximate the current as such:

$$I \cong I_s \exp\left({\beta(V - IR)}/{n}\right) \tag{3.18}$$

$$V \cong IR + \frac{n}{\beta}\ln(I) + n\phi_B - lnAA^*T^2 \tag{3.19}$$

$$\frac{dV}{dlnI} \equiv I\frac{dV}{dI} = IR + \frac{n}{\beta} \tag{3.20}$$

where n is the ideality factor. Then, one plots (dV/dlnI vs I) where the slope will correspond to the resistance of the device. Then, we go back to the CSM and repeat the process for each contact to plot R_T vs 1/Area. As an example of the analysis, we show the steps for the test structure for Al/(1.3 nm)LiF contact on an n-type Si substrate of resistivity $\sim 2.3\ \Omega cm$; first we measure the current response:

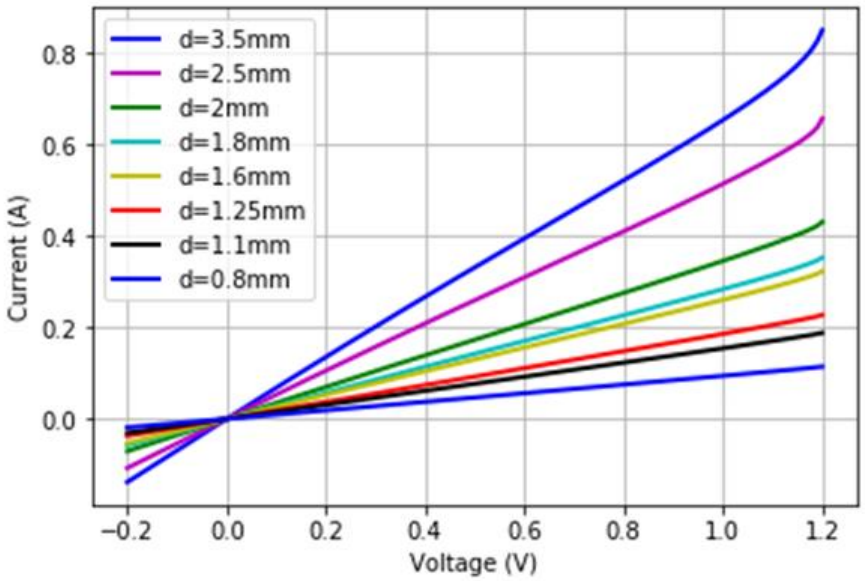

Figure 3.6 The I-V of 8 circular contacts of diameters 0.8mm to 3.5mm.

Next, we take the derivative of V with respect to I then multiply by I, since it is mathematically equivalent to taking the derivative of V with respect to the natural logarithm of I, and plot the result vs I:

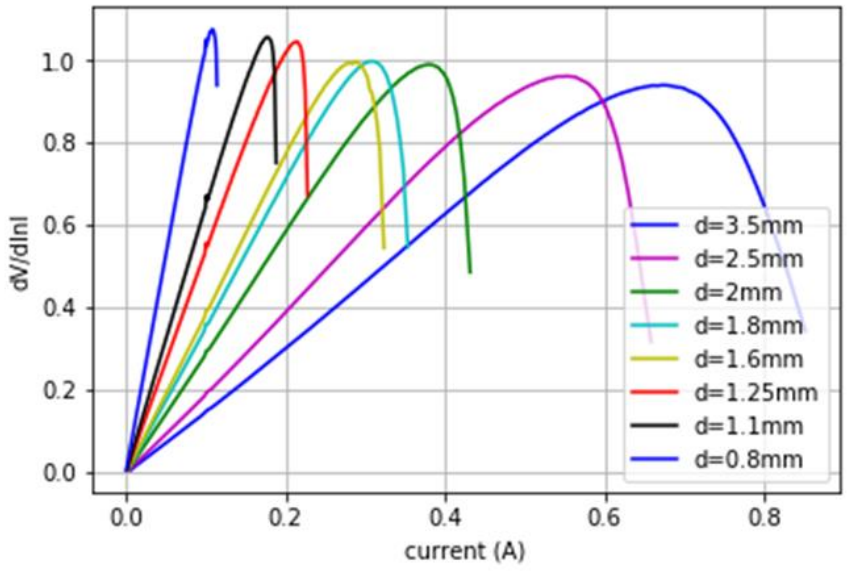

Figure 3.7 the first step of the analysis where dV/dlnI is computed and plotted versus the current, I.

As can be seen for ohmic contacts, such as the Al/(1.3nm)LiF on an n-Si substrate, the dV/dlnI vs I y-intercept is almost zero (Figure 3.7). The difference between considering whether the contact is ohmic or not can be quantified by this step, since we can always apply a linear regression to any set of points. In the last step, we plot R_T-R_S vs 1/Area such that :

$$R_T - R_S = R_C + R_0$$

$$R_T - R_S = \frac{\rho_C}{\pi d^2/4} + R_0 \tag{3.21}$$

As can be seen from Figure 3.8, the plot is linear when plotted according to (3.21). Such analysis (calculating R using the diode equation) could be applied to ohmic contacts, as well, and will produce extremely small n values.

In an error analysis paper that used finite-element analysis, it was shown that at low contact resistivity interfaces, the CSM overestimates ρ_C [76]. The paper also developed a different expression for the spreading resistance and suggested some guidelines to reduce the error in extracting ρ_C. One of the guidelines can be summarized as: make the resistivity of the substrate as low and comparable to ρ_C as possible. Since in this region, the 3 series resistors model is valid. When $\rho_C \cong 0.1\,\rho_w t$, the error is in ρ_C is less than 5% for the original CSM expression for spreading resistance. Thus, we moved to using 200 μm thick n-Si wafers with $\sim 0.8\,\Omega cm$ resistivity (thinner and less resistive wafers).

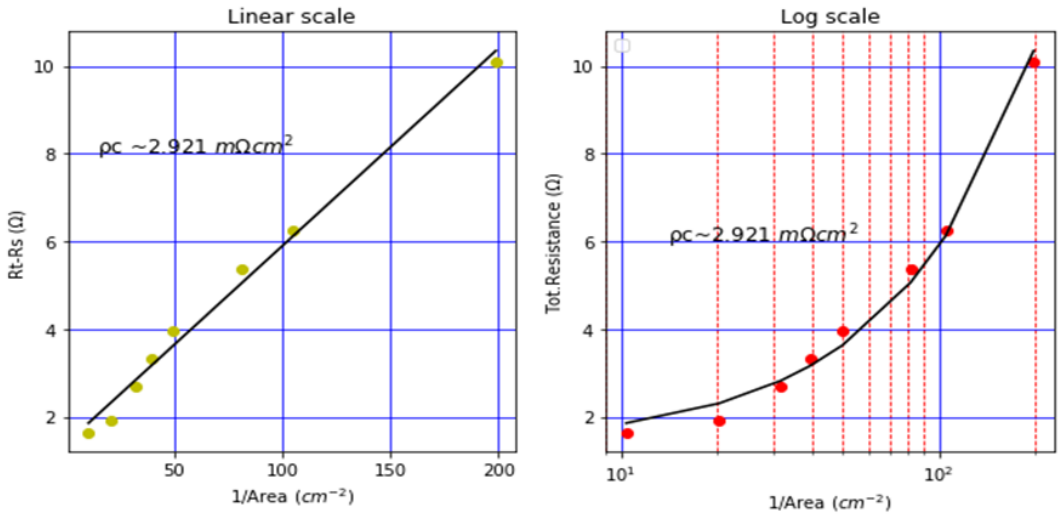

Figure 3.8 On the right, we have the total resistance calculated from the previous step, while on the left we remove the calculated spreading resistance from each contact correspondingly.

3.2.3.2 Barrier Height Measurement

Although there are other techniques such as capacitance-voltage measurements and spectroscopy-based methods, we can use I-V measurements to extract the barrier height as well, which requires a simpler setup. One could use Cheung's analysis for extracting the barrier height, as well. Starting from the diode equation, we extract the resistance, by taking the derivative of V as shown in CSM, and n from the dV/dlnI-I curve (Note: J and I may be used interchangeably in this analysis). Then we define a function H(I):

$$H(I) \equiv V - \left(\frac{n}{\beta}\right) ln(\frac{I}{AA^{*}T^{2}})$$

(3.22)

Such that

$$H(I) = IR + n\phi_B$$

(3.23)

Where we plot H vs I to extract R again and the intercept will be $n\phi_B$ where we have found n from the previous plot. The consistency of the analysis can be tested by comparing the first R with the second. For some reason, extracting R from JdV/dJ plots is more consistent than the one extracted from dV/dlnI plots, although they should be mathematically identical (Figure 3.9). As an example, we apply the analysis to the Ag/3nm of LiF/n-Si contact having the structure shown in Figure 3.5:

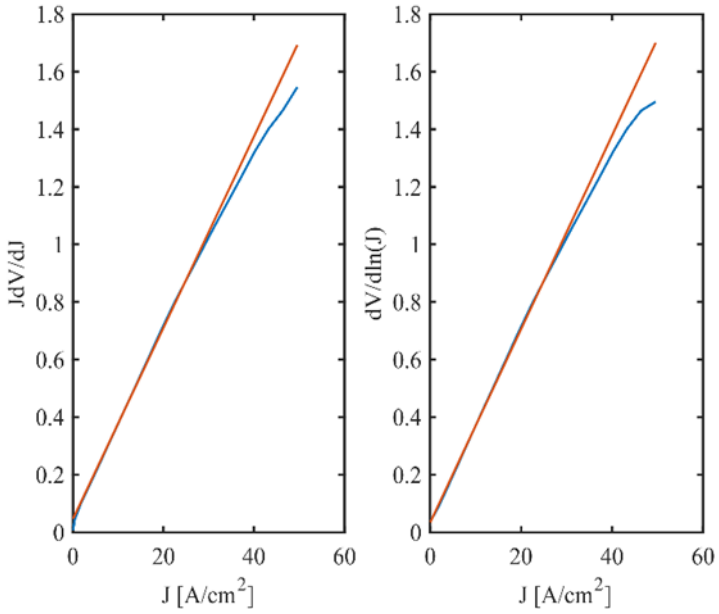

Figure 3.9 As can be seen from the computed derivatives, the difference is negligible. However, both plots provide slightly different resistance values along with different ideality factors. The effect of the different ideality facts can be seen in the H(J) plot.

Comparing both models, we can see both are almost identical to the experimental data (Figure 3.10). However, since we are modelling for 3 numbers simultaneously (R, n, and ϕ_B) we opt for the more consistent model, that is, model 1, whose values are: R $= 6.61\Omega$, $n = 1.8$, and $\phi_B = 0.53\ eV$. The high ideality factor indicates that a mechanism other than TE is active [79].

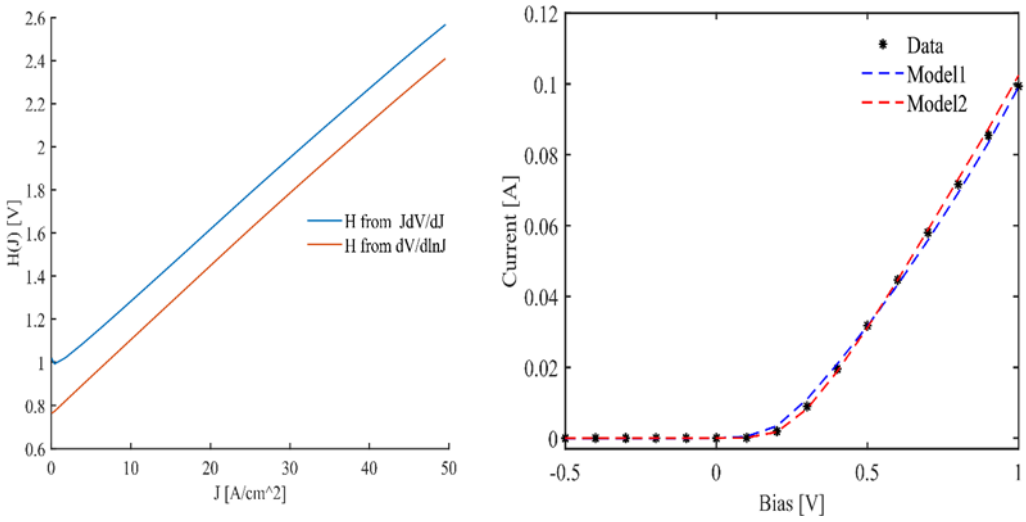

Figure 3.10 The difference in computed R for JdV/dJ is 0.0071 Ω. For dV/dlnJ it is 0.1184 Ω. thus, we use the ideality factor produced by the first method. It should be noted that plotting H(J) or H(I) does not cause a difference. Using the results of the analysis using 2 different derivatives show small differences. Model 1 used JdV/dJ, while model 2 used dV/dlnJ.

3.2.4 1-Sun and External Quantum Efficiency (EQE)

The 1-sun simulator is a device that mimics the operating environment of solar cells by placing the sample cell under a source with the optical spectrum of the sun having an intensity of 1 kW/m^2. The sample cell is put under such illumination and a bias voltage scan is applied to find the open-circuit voltage (V_{OC}) and its current response.

EQE

Due to the fact that the 1-Sun simulator retrieves current values, it needs to be corrected for the area to express our results in terms of current density. The main method to do so is through EQE measurements. Thus, we can retrieve the correct short circuit current density and calculate the correct efficiency of our samples.

EQE is defined as the ratio between the generated charge carriers that left the solar cell and incident photons [80]. EQE may also indicate which recombination losses are limiting the performance of the solar cell, where the UV/blue region is mainly affected by the front side, while the red/IR region is affected by the rear side .

CHAPTER 4

RESULTS & DISCUSSION

4.1 Experimental Results

Based on the observations done over the past decades, it is evident that an IL intended for the enhancement of current across the MS interface should possess certain features:

1. High Ionicity on Phillips' scale.
2. Large band gap.
3. Low defect formation energy.
4. Nanoscopic.

Accordingly, we decided to explore the applicability of thermally evaporated sodium chloride (NaCl) and sodium fluoride (NaF) as prospective ILs for c-Si solar cells. Under proper optimization (which is outside the scope of this thesis), these materials could prove more economic due to their abundance in nature, especially NaCl. The preemptive venture into tackling the abundance issue reveals itself in the solid-state battery industry where research is partially dedicated to exploring sodium as a replacement for lithium [81]–[83] .

4.1.1 XRD

For XRD measurements, we used the Rigaku Ultima-IV X-ray diffractometer which possesses automatic alignment for grazing angle analyses. Thin films of NaCl and NaF; of varying thickness between 5-100 nm, were deposited on c-Si (Fz (100), DSP,

thickness 200 µm) and glass substrates, by thermal evaporation at room temperature. NaCl or NaF powder (99.99%, pure) were used as the source material.

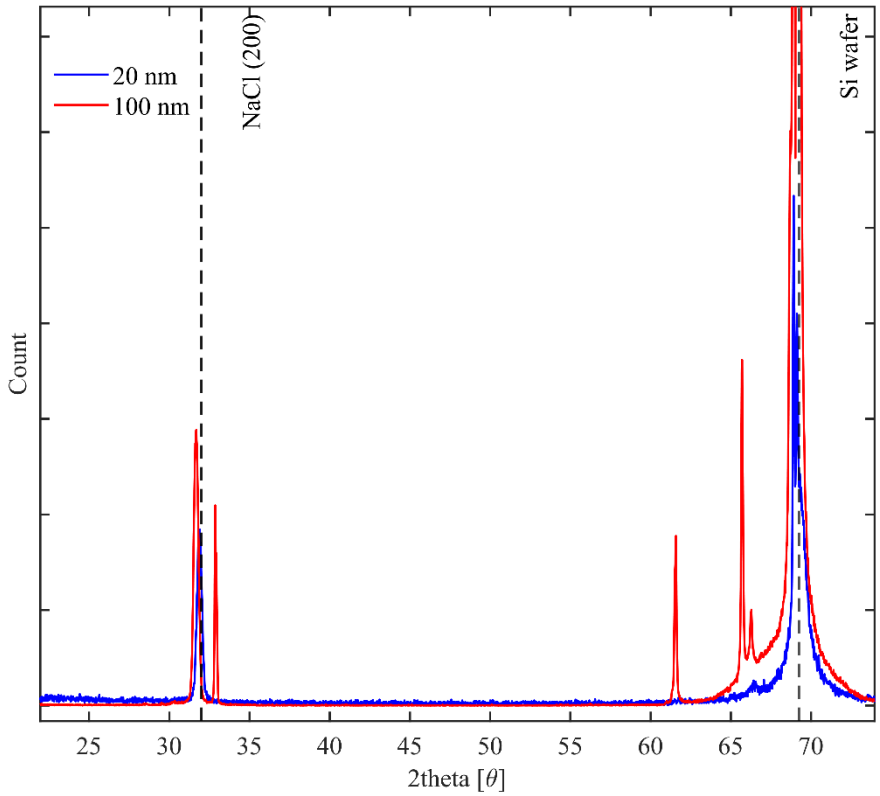

Figure 4.1 XRD results of NaCl deposited on a clean Si wafer. For two thicknesses we can see certain spikes corresponding to the NaCl. However, for the 20nm, there is practically only one peak that corresponds to the 200 direction.

The base pressure was 1-5×10^{-6} Torr. The c-Si wafers were cleaned by RCA/RCA2 followed by HF dip before loading into the thermal evaporation system. XRD diffraction revealed that the 20 and 100 nm thick NaCl (Figure 4.1) and 100 nm NaF (Figure 4.2) exhibit single peaks in the (200) direction for NaCl (at 32°) and [100] for NaF (at 39°). Samples with layers of thicknesses lower than 20 nm did not show peaks other than that of the substrate. This does not necessarily mean that 20 nm is the threshold at which the layer becomes crystalline. For NaCl, another group made the same observation that only a single peak exists, at least for layers of 100nm or below [84].

For the silicon substrate we can see that the silicon peak dominates but there are other peaks around angles 62 and 67. We could conclude it belongs to the NaCl layer, however, the same peaks appear for the NaF layer (Figure 4.2). As for the peak at 33 degrees, it is referred to as the Si (200) forbidden peak. The origin of its occurrence is most likely that the sample has a non-zero in-plane angle [85]. It is interesting to note that in the case of not applying HF, those peaks (at 62° and 67°) were stronger and other small peaks appeared.

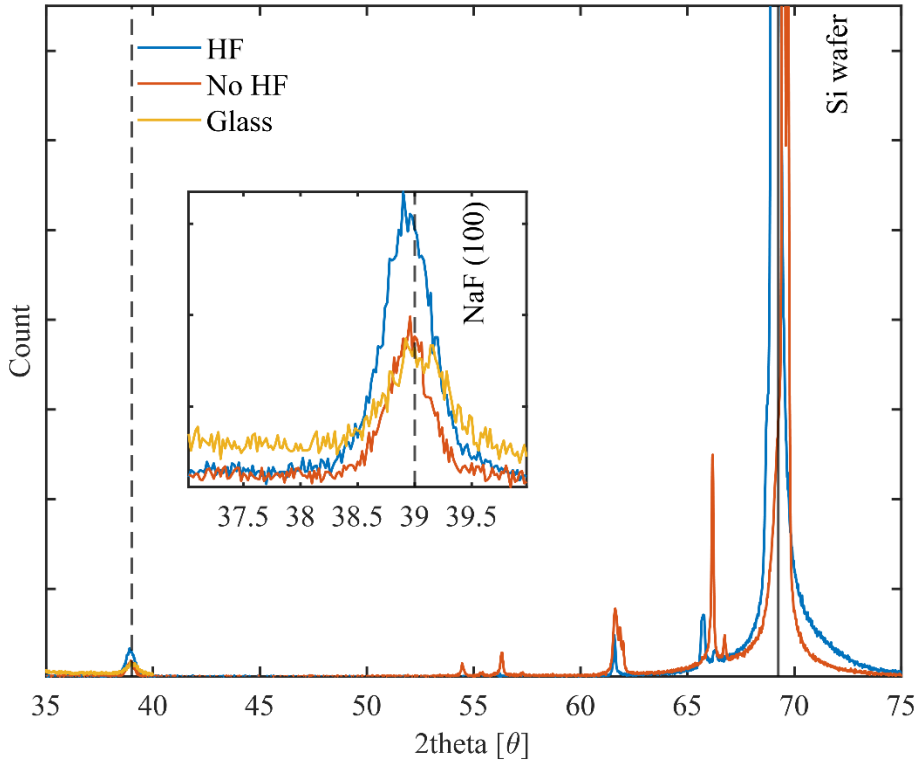

Figure 4.2 XRD results for 100 nm NaF on different substrates. It can be seen that in the case of glass substrate and not applying HF does not cause the peak to differ much in strength.

The HF/no HF comparison tells us the substrate's crystallinity boosts the crystallinity of our layer, since without applying HF, NaF is being deposited on amorphous silica. This may be relevant, later.

4.1.2 Dark I-V measurements

We prepared circular contacts of the same radius using shadow masks. The ILs and metals were deposited without breaking vacuum under 1 μTorr on 200 μm thick DSP n-Si <100> with resistivity of approximately 0.8 Ω.cm. In the first set of experiments, we fixed the IL and changed the metals and in the other we varied the IL. In another set of experiments, we extracted the contact resistivity using CSM for LiF, NaF, and NaCl IL capped with Al. Finally, we verify the selectivity qualitatively by changing the majority charge carrier in the substrate. For the first set of experiments, It can be seen from Figure 4.3 that adding LiF effectively removed the pinning effect observed for the Metal/Si contacts (i.e., SBH now depends on ϕ_m).

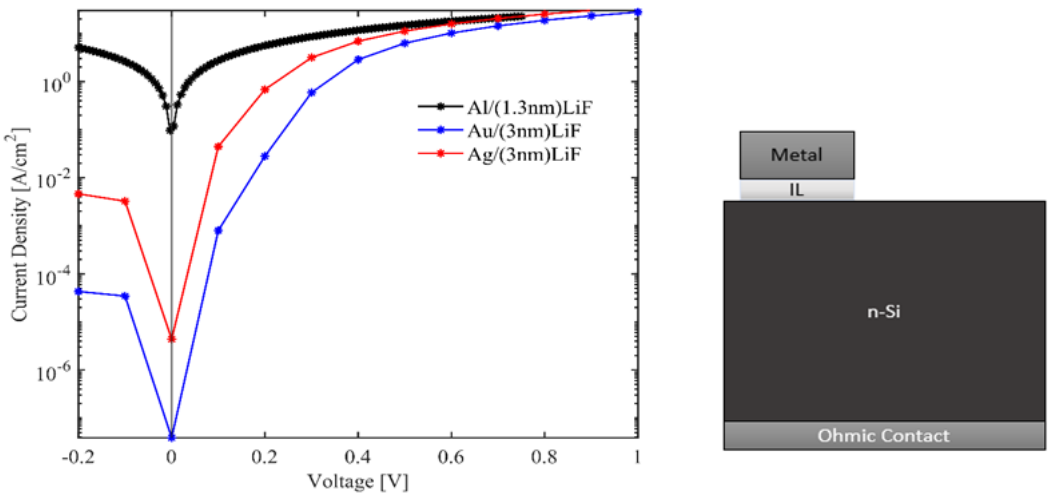

Figure 4.3 IV measurement of Al/LiF/Si, Ag/LiF/Si, and Au/LiF/Si where the contact diameter was 0.6mm for the Ag and Au contacts and 0.8cm for the Al contact. The higher reverse current in the case of Ag/NaF is indicative of a lowered barrier. After forward bias of 0.6V the current becomes dependent on the system's resistance.

For the Al/LiF contact, we deposited 1.3 nm only to have an effective workfunction (~3 eV at this thickness) comparable to the other contacts(~3.8 eV). In literature, the success of LiF as an IL in c-Si solar cells has been attributed to different causes. The main three hypotheses, summarized by J. Bullock et al. [86] regarding the enhancement of current due to adding LiF as an IL are as follows:

1. Lithium chemically dopes the surface of the semiconductor, in this case Si.

2. Protection from Al at the surface of Si.
3. The extremely low work function value of the Al/LiF interface.

For the first hypothesis, it was concluded that it could not be the case as the LiF layer was shown to be stable through STEM imaging [86] such that Li did not diffuse in the Si substrate. S. Wan et al. also have shown chemical inertness of the LiF/Si interface [87]. The second hypothesis relies on the MIGS explanation; as LiF is acting as a region of no electrons, the gap states of Si cannot be filled by the Al electrons since they are screened by the distance. The third hypothesis goes in line with R. Schlaf et al.'s experimental results and others [63][26]. Although Zhengyi Sun et al. [26] showed that the effective work function of coinage metals (Cu, Ag, Au) was 3.8 eV upon depositing 3nm of LiF, the barrier height of such contacts is actually different. This shows that that the effective work function is not the only cause for enhanced electron transport across such interface. It must be a combination of reduced MIGS at the interface and an effective work function and potentially in combination with other surface parameters, like orientation.

On the other hand, when using Cheung's analysis on the Au/LiF contact, it produced an ideality factor of approximately 0.2 which led to a high barrier height of 1.26 eV, which is somewhat unreasonable. Using the formula relating the BH to the saturation current density:

$$\phi_B = \frac{kT}{q} ln\left(\frac{A^* T^2}{J_{sat}}\right) \tag{4.1}$$

the BH for the Au/LiF contact was found to be 0.663 eV, while for Ag/LiF it is 0.55 eV (0.584 eV using Cheung's analysis). The discripancy between Cheung's analysis and the reverse saturation current is most probably due to the small number of data points in the forward bias region such that the numerical derivative was not well defined, and not accounting for the image-effect that diminishes the barrier in the reverse bias.

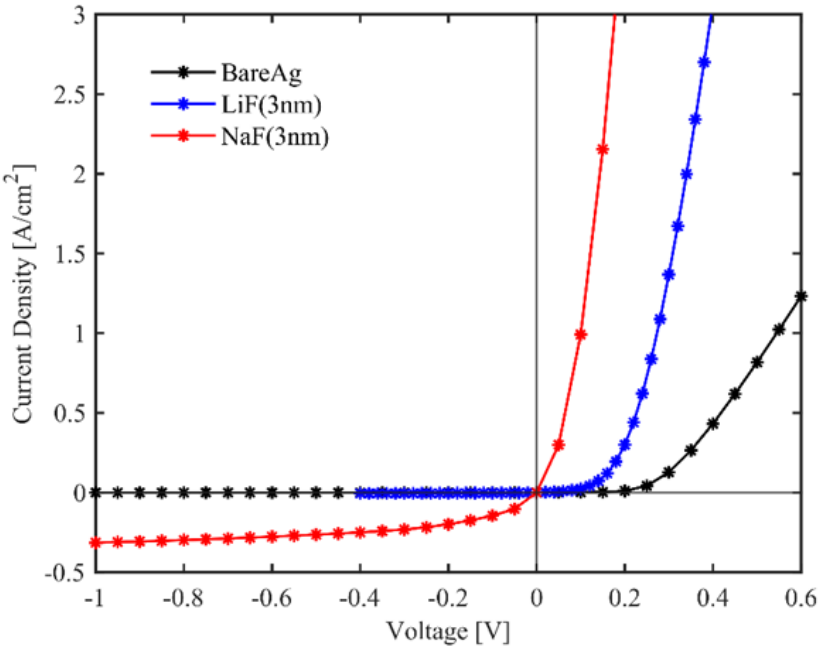

Figure 4.4 Using the same structure as in the previous figure, we compare the performance of NaF with LiF for Ag contacts on n-Si.

Next, we compare the performance of using our proposed material with using LiF. Although LiF has the largest known bandgap, both experimentally and numerically, NaF still outperformed it in lowering the barrier height at the Ag/n-Si interface (Figure 4.4). The outperformance can be attributed to the slightly higher ionicity of NaF on the Phillips' ionicity scale.

Table 1 Extracted effective SBH of different contacts on the same substrate (n-Si).

Contact Structure	Barrier Height (eV)
Bare Ag	0.698
Ag/LiF	0.584
Ag/NaF	0.472

4.1.3 Charge-Carrier Selectivity

Next, we show the charge-carrier selectivity by comparing the current response of the contact on substrates of different doping type. Due to the extremely high ionization energy (VBM) of the alkaline halides, we expected NaF to be electron selective such that when the substrate has holes as the majority charge carriers it, the current response becomes rectifying. Our expectation is justified by the large band gap that such material possess such that the tunneling probability is diminished for holes and due to the unpinning there will be a thermionic barrier that the holes must overcome. This naturally leads to valence band offset larger than that of the conduction band offset, which primarily cause the selectivity. This is visible in Figure 4.5.

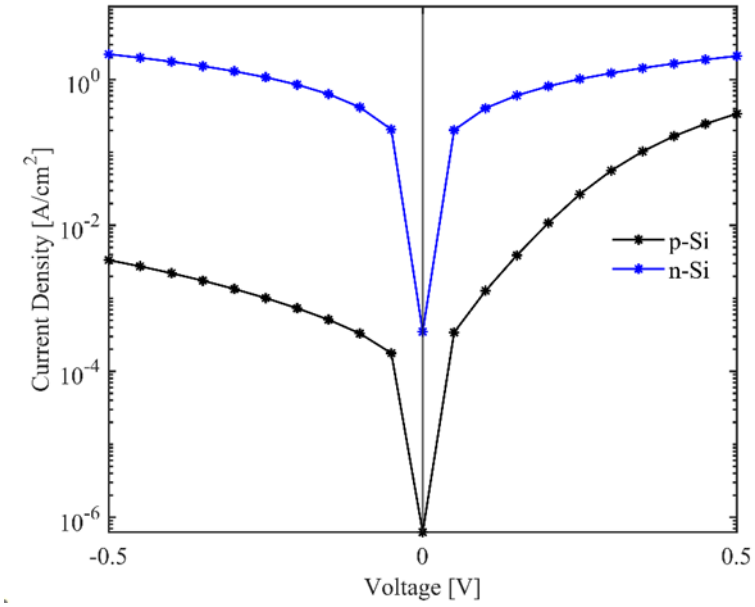

Figure 4.5 J-V measurement of Al/NaF(5nm) on different substrates. It can be seen that for the p-Si substrate, there is a saturation current corresponding to an effective barrier height of 0.619eV. However, one cannot use the TE model to quantify the barrier across the Al/NaF/p-Si interface.

Following Sze's use for Richardson's constant; for the p-type substrate we used a value of 30, while for the n-type substate whose orientation was <100>, we used a value of 120 in order to deduce the barrier height from the forward direction current. The barrier deduced is really an effective one, which reveals itself in the ideality

factor deviating from $n = 1$ [79]. This is a sign that the barrier is field-dependent and that tunneling is occurring alongside with TE, which is expected.

4.1.4 Contact Resistivity Measurement

We used CSM to extract the contact resistivity of Al/IL/n-Si contacts (IL= LiF, NaF, NaCl) by making contacts with different radii. From Figure 4.6, we Note that NaF and NaCl outperformed LiF in the range of thicknesses tested, which were calibrated by spectroscopic ellipsometry with a resolution of ± 2 Å. We may conclude that the size of the bandgap is not the only factor causing the IL to have high electrical performance. This is because, NaF's bandgap is approximately 11.4 eV, while for NaCl and LiF, it is 9.5 eV and 13.6-14.2 eV, respectively [88].

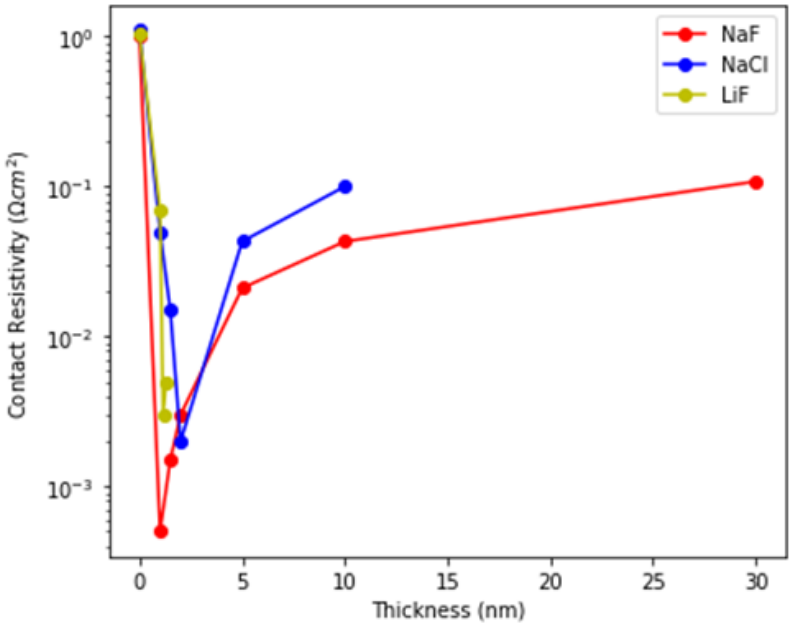

Figure 4.6 The extracted contact resistivity using the CSM analysis for different IL thicknesses of NaF, NaCl, and LiF.

The dependency of contact resistivity on thickness can be understood from the transport mechanism, which is a combination of TE and FNT. The TE model tells us how many electrons have energy enough to move across an energy barrier. The tunnelling barrier tells us the likelihood of an electron passing a barrier, depending

on its energy. Thus, the current across the contact should, approximately, be the likelihood of electrons that passed the energy barrier to pass the tunnelling barrier:

$$J_{tot} \cong \Theta J_{TE}$$

Where Θ is an overall tunnelling probability, which is inversely proportional to exponent of the root of the thickness of IL (by defining the electric field in the FNT expression as $E = V/d$), for a given bias voltage. This is a simplistic view of electron transport across such junctions. However, it qualitatively accounts for the behaviour seen in Figure 4.6, between 1-10 nm. After this thickness range, one could model such layers as capacitors [5], [86].

4.1.5 EQE and 1-Sun Results

Finally, we try utilizing the IL in a n-Si solar cell at the backside as shown in Figure 4.7. The front side's optimization was done by another team, where SiN_x passivation, texturing, and Boron surface doping were implemented with Ag/Al paste front contacts.

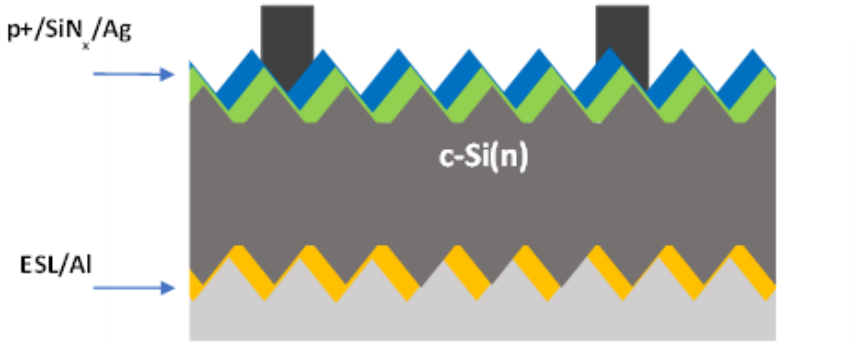

Figure 4.7 Schematic of the solar cell structure. At the front, we have surface doping, creating a thin p+ layer passivated with SiNx and metal capped with silver. At the back, we deposited the IL dubbed ESL short for electron selective layer.

The EQE results shown in Figure 4.8 revealed almost identical behavior throughout the spectrum for the three IL, which was expected. In the inset graph, we can see how the cell with NaF had higher EQE, fractionally, throughout the spectrum except for the UV region. Whereas NaCl was identical to LiF, it showed slightly lower

efficiency in the IR region indicating slightly higher surface recombination relative to both NaF and LiF.

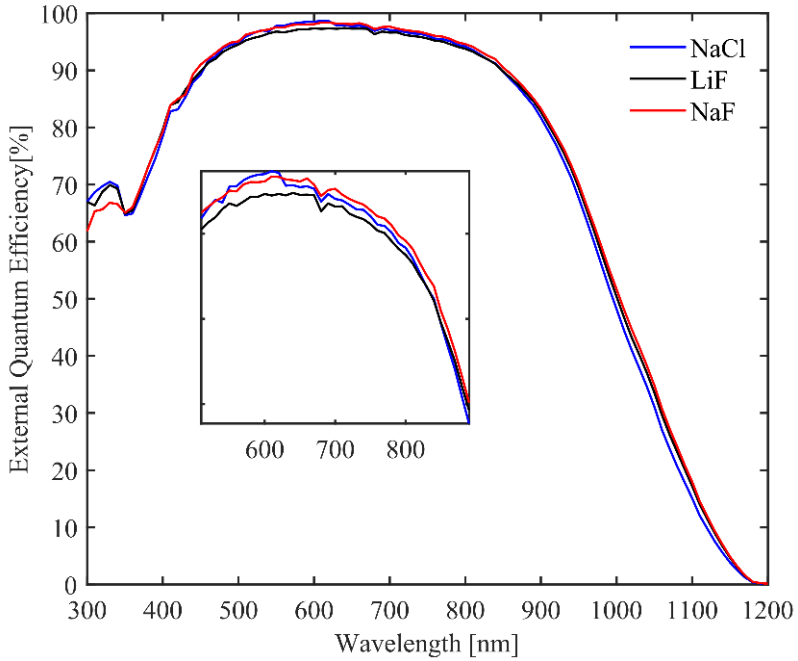

Figure 4.8 EQE results for the champion cells with different layers implemented at the backside capped with Al as the metal contact.

Table 2 Results for the n-type solar cells after the EQE corrections.

Contact	V_{oc} (mV)	J_{sc} (mA/cm^2)	FF (%)	Efficiency (%)
NaCl (2 nm)	581.4	35.48	78.7	16.23
	581.2	35.63	79.1	16.38
NaF (~1.5nm)	**591.2**	**36.07**	**81.13**	**17.30**
	591.2	35.85	79.22	16.79
NaF (1.5 nm)	586.3	35.40	78.59	16.31
	591.3	35.88	78.11	16.57
LiF (1.8 nm)	591.3	35.44	78.84	16.52
	591.3	**35.72**	**80.62**	**17.03**

In Table 2, the results of the sample cells are summarized, after the EQE correction. Since deposition was done on textured surfaces, the optimum thicknesses did not

exactly correspond to the ones from contact resistivity measurements. Figure 4.9 shows the current density response of the champion cells for each layer, ceteris paribus. Given that the cells based on LiF were reported to be at above 19% efficient and could go up to 23% efficient with proper passivation, and that NaF was slightly better than LiF in our tests, NaF should perform better under the same circumstances.

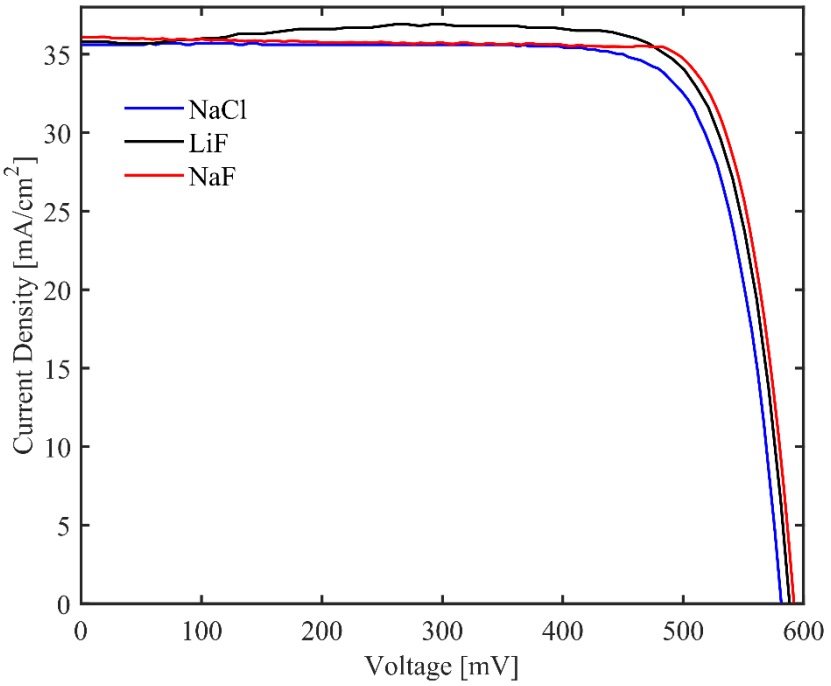

Figure 4.9 The J-V results of the solar cells, having average area of 2x2cm^2, with different ILs after the EQE correction of the short circuit current density.

4.2 Discussion

The XRD indirectly shows how after a certain thickness the ionic crystals become crystalline. This is quite interesting as the crystals do not need a crystalline substrate for the atoms to arrange themselves after a certain thickness. This is not seen in most evaporated solids. This further corroborates Frenkel's analysis of ionic surfaces.

Since J. Bullock et al. [6] has shown, indirectly, that 3 of I-VII crystals act almost identically in the IL regime, we may start with LiF as it has been studied the most among the ionic crystals as an IL since L.S. Hung's work [4]. Based on a band gap

of 12-14.5 eV [4], [87]–[89] and ionization energy of 11.3 eV [63] , we may draw the band diagram of LiF [100] and compare it with what happens upon contacting another crystal.

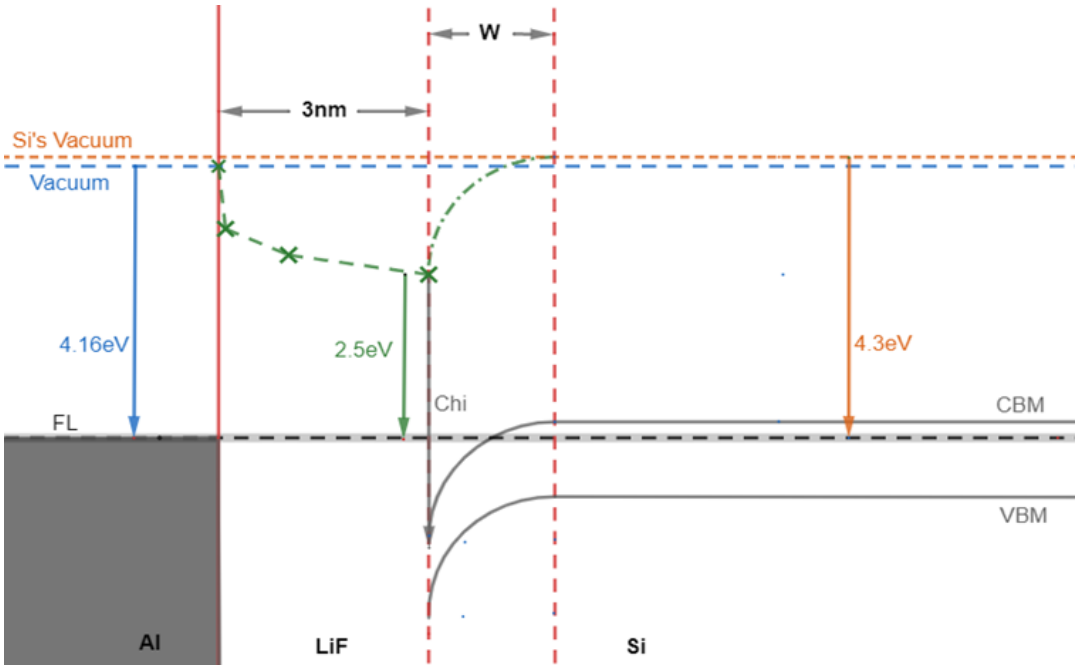

Figure 4.10 Schematic of the band diagram of the Al/LiF/n-Si interface.

In Figure 4.10, outside the metal, we see the experimentally demonstrated lower work function of Al/LiF_x [63] for 3 nm coverage. It has been attributed to a dipole layer [63][4][5]. This is true to an extent, however calling it a dipole layer is misleading since a dipole layer is an electrostatic configuration that will not continue to exist if time is allowed to pass. Since the interface is chemically inert for LiF_x/n-Si [87], the CBM of Si must remain at 4.05 eV below vacuum at the interface.

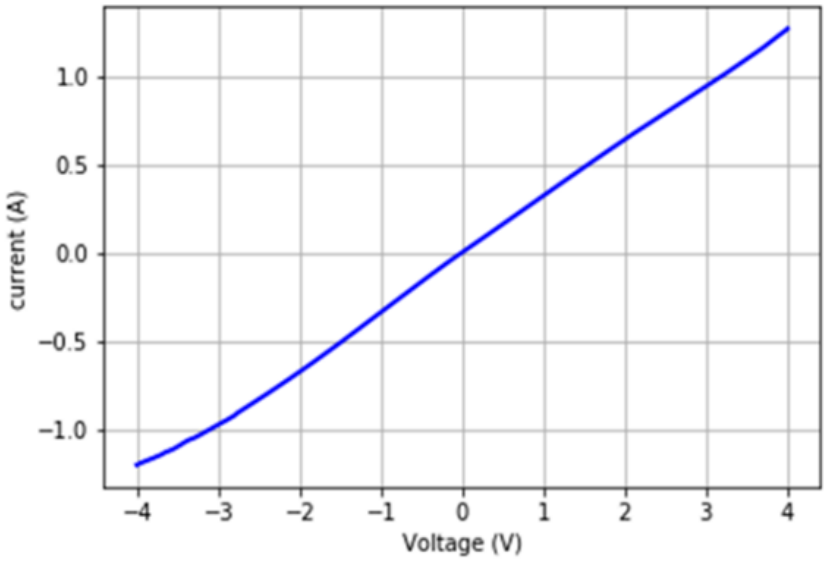

Figure 4.11 The IV result of Al/(2nm)NaCl/n-Si. The device structure is similar to the CSM structure where the front contact is a circular contact of radius 1.7mm and the back contact is fully covered and ohmic.

This causes accumulation to occur to an extent that Si acts as degenerately doped Si near the interface. This is justified by the range over which such contacts (ionic crystals as IL) are Ohmic in the reverse bias, as in the case of Al/2nm NaCl where the contact was ohmic up to -4 V (Figure 4.11). Now, in this case, on either side of the IL the CBM should be below the FL such that the band diagram is symmetric about the contact. Analytically, it was shown that for a FN-type barrier the tunnelling probability is the same whether the electron is leaving the emitter or entering it from vacuum [90], which may be generalized for smooth barriers. This corroborates the picture that when tunnelling is the dominant mechanism of current transport across the contact, the device appears ohmic. This is because the contact, after a fractional bias, passes more electrons than the substrate can pass. Furthermore, if the CBM were to be above FL by anything below 0.3 eV ($\phi_B \leq 0.3eV$) it would not have shown in the analysis due to the parameters under which the current was measured.

Next, in the case when the metal is Ag and Au (higher work function), we can look at the interface as being composed of two cascading barriers, that of the IL and the band bending caused by the mismatch in FL before contact. The theoretical electron SBHs for Ag ($\phi_m \sim 4.6\ eV$) and Au ($\phi_m \sim 5.3\ eV$) [26] is $0.55\ eV$ and approximately

1.25 eV, neglecting the image effect. However, by the inclusion of LiF or similar ionic crystals, the work function of the surface becomes 3.8 eV, approximately. Although Au and Ag possess the same effective work function upon depositing the same thickness of LiF, their J-V response is not the same which implies that the inherent workfunction of the metal somehow acts as a parameter, since the difference between Ag and Au's electronic densities is negligible. This further validates the lack of FLP at the interface.

In terms of quantifying observations, the most effective theories are still TE and FNT, where the former ignores the exact origin of the barrier height, and the latter simplifies its shape to that of a triangle (ignoring the image-effect). In the case of TE, one can always model any rectifying contact and establish an effective barrier, which would encompass other conduction mechanisms that partially appear in the ideality factor (n). If n does not deviate much from unity, TE is enough to effectively characterize the MS interface [79].

As for FNT, R. G. Forbes [39] pointed out that a good portion of the literature is neglecting the image-effect correction (Schottky-Nordheim tunnelling (SNt)) presented in the fifties [21], which was shown to be of significance, especially in nonplanar emitter surfaces. Although the difference between SNt and FNT amounts to a correction factor [37], this correction factor is electric field-dependent in case of nonplanar emitters. A perfectly planar surface is quite rare. The correction factor if not accounted for, will convolute the measured barrier. This may be one of the causes, on top of surface morphology and measurement techniques, as to why some report different ϕ_M and ϕ_B values for metals and interfaces of similar crystallinities and bulk properties, respectively, in the literature.

The manner in which the tunnelling barrier and the thermionic barrier are resolved is usually done through temperature dependent IV measurements. As the temperature

goes down, TE is suppressed while the tunnelling current remains constant [77]. Unfortunately, the system was not available for further analysis.

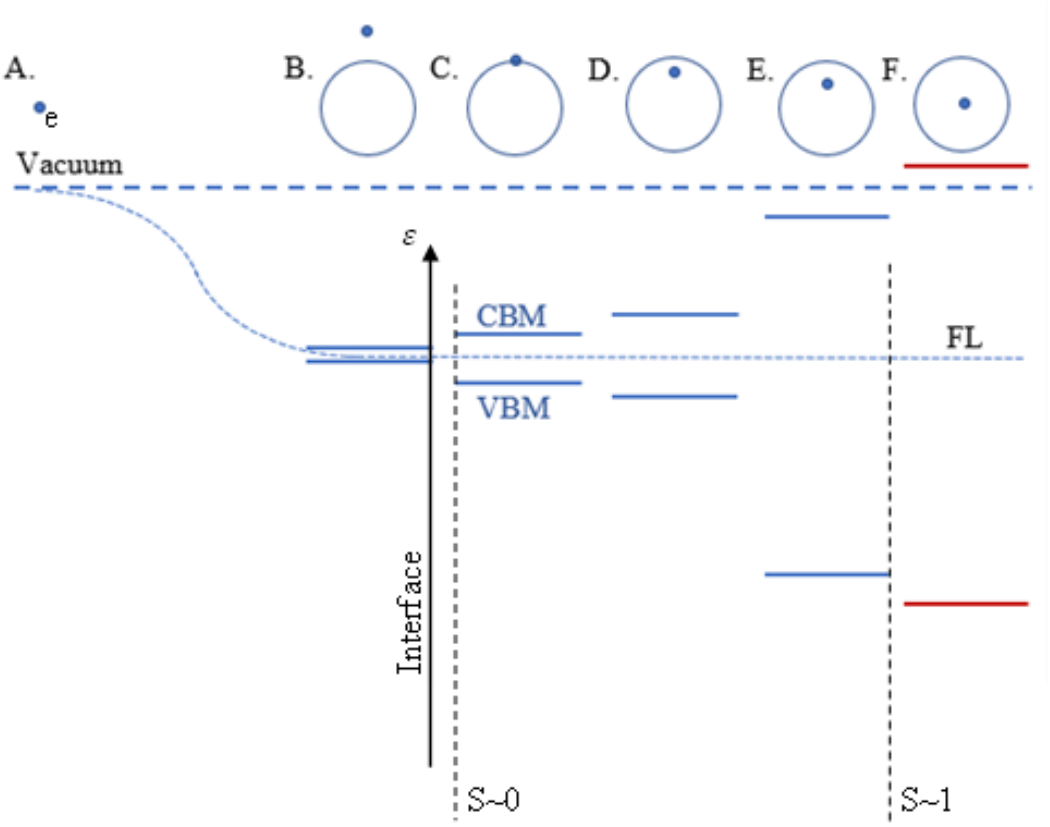

Figure 4.12 A Schematic of the band structure an electron perceives in a single direction in a periodic structure. A. Vacuum, no structure. B. A metal where the band gap is of the order of thermal voltage or less. C-E Group IV and binary crystals. F. Ionic crystals, characterizable by different phenomena including negative electron affinity, i.e., the CBM is above vacuum level. Note: the FL is not always the same distance from vacuum, as it can vary from 2-6eV. At the top, circles signify degree of localization near the parent ion. At the bottom, we see the scale of degree of FLP.

The studies done on metal/non-metal contacts show the trend of moving towards the SL with increasing bandgap/ionicity through contact resistivity measurements and their functionality as Si-based solar cells [5], [8], [10], [11], [14], [35], [91]–[94]. Schlaf et al. and others have also revealed that the MI interface exhibits relatively lower metal work function. One can summarize the observations done throughout the decades as shown in Figure 4.12. We see how when we move from vacuum to a structure of very weak periodic (practically, most metals), the continuum of states is not fully accessible (Chapter 2). As we go from left to right, the periodic potential goes from non-existent, in vacuum, to extremely strong, in ionic crystals, as evident

from the huge bandgap. Exact accounting for the different weights of interface mechanisms is almost impossible, right now. This is due to errors in the metal work function extraction, different topology of surfaces studied in literature over time, and unaccounted substrate effects that include substrate thickness and resistivity. However, it is evident that for ionic crystals, unlike Si and Ge, electrons are well localized such that, at the surface, the ions become freer to move, instead of generating extra electronic states in the forbidden region as a response to lattice termination. Here is a set of strategies that will enhance MIS-based contacts:

Frenkel/Gibbs picture: for ionic crystals, it is evident that band bending is occurring because of the difference in the Gibbs free energy of defects allowing ions to move more freely at the surfaces and acting as dipoles in the sub-nanometer regime. If the moving ions are participating in the conduction, then using impure (doped) ionic crystals will increase the density of defects hence enhancing the field effect present in these layers[95]–[97].In addition to this, thermodynamically, defects generated by high substrate temperature may be partially frozen by capping. Thus, experimenting with substrate temperature during deposition may reveal contacts with superior electronic properties.

Bardeen/Tersoff/Heine picture: As MIGS qualitatively explains the observed partial depinning in silicides and germanides, and almost full depinning in the case of Bi/Si and Bi/Ge, the use of semi-metals could be used to further minimize the influence of gap-states in MIS contacts. MIGS could also be used to view IL as a screen [95], [97] thereby lowering the matching DOS that would pin the FL of Si near CNL.

CHAPTER 5

CONCLUSION

In conclusion, we found that adding an ultrathin layer of NaF or NaCl between Si and metals unpins the FL from around CNL such that the barrier perceived by the electrons is dependent on the metal work function. We attribute this to their ionic nature such that on the one hand they distance the metal from silicon, while, on the other hand, they possess no electronic states that matches that of silicon's unoccupied gap states to pin the FL. From Frenkel's analysis, the ions themselves spread at the surface of ionic crystals to achieve neutrality with bulk as opposed to forming dangling bonds to be filled in the case of covalent solids. This is another reason why such crystals have poor passivation quality.

Due to these layers' band structure, they act as electron selective layers, in the sense that they diminish the passage of holes by having a much larger tunnelling barrier. To this end, we utilized these layers as rear planar contacts in an n-Si solar cell and compared their performance to that of an optimized cell with LiF in their stead. NaF outperformed LiF by a slight margin (0.3%), ceteris paribus, achieving a power conversion efficiency of 17.3%. Since the enhancement was in the short circuit current density and fill factor, coupling the use of NaF with a better passivation at the front and optimized partial contact coverage at the back side offers guaranteed routes for improvement.

Finally, since we proposed and tested NaF and NaCl as ILs based on the experiments and several existing models explaining some of the isolated features of solid-state surfaces, and their success in lowering the contact resistivity of Metal/Si contacts up to 3 to 4 orders of magnitude without sophisticated contact strategies, we propose a set of materials that can also function as IL in contact design where contact resistivity

is minimized: beryllium oxide (BeO), strontium fluoride (SrF_2), and silver iodide (AgI). Qualitatively, any transparent crystal would partially unpin the FL as an ultrathin IL.

Choosing the parameter that dictates which ionic crystal would outperform the other is tricky. Although NaF has a smaller bandgap, it outperformed LiF as an IL in terms of current density in rectifying contacts and contact resistivity in ohmic contacts, which tells us that the size of the bandgap is but a parameter for superior contacts. The only scale that consistently correlated with the reported contact resistivity values, both in this thesis and in literature, was the ionicity scale. It is even correlated with the degree of pinning. Unfortunately, Philips' scale lacks generality since it was made for binary crystals without accounting for d or f valence electrons. This limits its usability in predicting the performance of other more complex ionic crystals in the IL regime, e.g., lithium niobate's ionicity is undefinable (in Philips' model), because niobium has d electrons, and the crystal is not composed of a binary compound.

As for a strategy, the contact should incorporate an optimized combination of both pictures (the ionic surface and MIGS). Combining both the MIGS picture and the Frenkel picture, we are led to conclude that depositing a semi-metal, with an appropriate work function, between the IC and the metal is the best strategy in terms of minimizing the contact resistivity of the contact. Thus, for n-type semiconductors: Al/semi-metal/IC/S is potentially the ultimate recipe for minimal resistance, where the thickness of the semi-metal is on the order of 10 nm (as they are more resistive than metals). However, the thickness should be enough to completely eliminate the influence of the MIGS from partially pinning the FL.

As an example, for n-Si, adding a few nanometers of Bi between Al and the ionic IL should further reduce the MIGS at the interface, while unpinning the FL through the mobile ions in the IC. Implementing this exact combination of Al/Bi/IC/S may have varying outcomes for different c-Si orientations, not to mention other

semiconductors. This is mainly due to how different layers have varying passivation effects depending on the substrate, which is beyond the scope of this thesis.

REFERENCE

[1] S. CHAPMAN, “William Gilbert and the Science of his Time*,” *Nature*, vol. 154, no. 3900, pp. 132–136, Jul. 1944, doi: 10.1038/154132a0.

[2] “S.M. Sze - Physics of Semiconductor Devices-John Wiley and Sons (WIE) (1981)”.

[3] “John David Jackson - Classical Electrodynamics (1999, John Wiley) - libgen.lc”.

[4] L. S. Hung, C. W. Tang, and M. G. Mason, “Enhanced electron injection in organic electroluminescence devices using an Al/LiF electrode,” *Appl Phys Lett*, vol. 70, no. 2, pp. 152–154, Jan. 1997, doi: 10.1063/1.118344.

[5] J. Bullock *et al.*, “Efficient silicon solar cells with dopant-free asymmetric heterocontacts,” *Nat Energy*, vol. 1, no. 3, p. 15031, 2016, doi: 10.1038/nenergy.2015.31.

[6] J. Bullock *et al.*, “Stable Dopant-Free Asymmetric Heterocontact Silicon Solar Cells with Efficiencies above 20%,” *ACS Energy Lett*, vol. 3, no. 3, pp. 508–513, 2018, doi: 10.1021/acsenergylett.7b01279.

[7] J. Bullock *et al.*, “Dopant-Free Partial Rear Contacts Enabling 23% Silicon Solar Cells,” *Adv Energy Mater*, vol. 9, no. 9, pp. 1–6, 2019, doi: 10.1002/aenm.201803367.

[8] K. Gao *et al.*, “Progress and Future Prospects of Wide-Bandgap Metal-Compound-Based Passivating Contacts for Silicon Solar Cells,” *Advanced Materials*, vol. 34, no. 26, p. 2200344, Jul. 2022, doi: 10.1002/adma.202200344.

[9] G. Du *et al.*, “High-performance hole-selective <scp> V $_2$ O $_X$ </scp> / <scp> SiO $_X$ </scp> / <scp> NiO $_X$ </scp> contact for crystalline silicon solar cells,” *EcoMat*, vol. 4, no. 3, May 2022, doi: 10.1002/eom2.12175.

[10] Y. Wan *et al.*, “Magnesium Fluoride Electron-Selective Contacts for Crystalline Silicon Solar Cells,” *ACS Appl Mater Interfaces*, vol. 8, no. 23, pp. 14671–14677, Jun. 2016, doi: 10.1021/acsami.6b03599.

[11] Y. Wan *et al.*, “Conductive and Stable Magnesium Oxide Electron-Selective Contacts for Efficient Silicon Solar Cells,” *Adv Energy Mater*, vol. 7, no. 5, p. 1601863, Mar. 2017, doi: 10.1002/aenm.201601863.

[12] H. Nasser, M. Z. Borra, E. H. Çiftpınar, B. Eldeeb, and R. Turan, “Fourteen percent efficiency ultrathin silicon solar cells with improved infrared light management enabled by hole-selective transition metal oxide full-area rear passivating contacts,” *Progress in Photovoltaics: Research and Applications*, vol. 30, no. 8, pp. 823–834, Aug. 2022, doi: 10.1002/pip.3510.

[13] H. Nasser, G. Kökbudak, H. Mehmood, and R. Turan, “Dependence of n-cSi/MoOx Heterojunction Performance on cSi Doping Concentration,” *Energy Procedia*, vol. 124, pp. 418–424, Sep. 2017, doi: 10.1016/j.egypro.2017.09.267.

[14] Z. Chen *et al.*, “Yttrium Fluoride-Based Electron-Selective Contacts for Crystalline Silicon Solar Cells,” *ACS Appl Energy Mater*, vol. 4, no. 3, pp. 2158–2164, Mar. 2021, doi: 10.1021/acsaem.0c02646.

[15] Y. Luo *et al.*, “Electron work function: an indicative parameter towards a novel material design methodology,” *Sci Rep*, vol. 11, no. 1, Dec. 2021, doi: 10.1038/s41598-021-90715-4.

[16] B. G. Streetman, • Sanjay, and K. Banerjee, “Global edition Solid State electronic devices Seventh edition.”

[17] N. Ashcroft and N. D. Mermin, *Solid State Physics*. Saunders College Publishing, 1976.

[18] J. Bardeen, “Surface states and rectification at a metal semi-conductor contact,” *Physical Review*, vol. 71, no. 10, pp. 717–727, 1947, doi: 10.1103/PhysRev.71.717.

[19] J. Tersoff’, “Theory of semiconductor heterojunctions: The role of quantum dipoles.”

[20] R. H. Fowler and L. Nordheim, “Electron emission in intense electric fields,” 1928. doi: 10.1098/rspa.1928.0091.

[21] E. L. Murphy and R. H. Good, “Thermionic Emission, Field Emission, and the Transition Region,” *Physical Review*, vol. 102, no. 6, pp. 1464–1473, 1956, doi: 10.1103/PhysRev.102.1464.

[22] A. M. Cowley and S. M. Sze, “Surface states and barrier height of metal-semiconductor systems,” *J Appl Phys*, vol. 36, no. 10, pp. 3212–3220, 1965, doi: 10.1063/1.1702952.

[23] V. Heine, “Theory of Surface States.”

[24] R. T. Tung, “The physics and chemistry of the Schottky barrier height,” *Appl Phys Rev*, vol. 1, no. 1, 2014, doi: 10.1063/1.4858400.

[25] J. P. Sullivan, R. T. Tung, M. R. Pinto, and W. R. Graham, “Electron transport of inhomogeneous Schottky barriers: A numerical study,” *J Appl Phys*, vol. 70, no. 12, pp. 7403–7424, Dec. 1991, doi: 10.1063/1.349737.

[26] Z. Sun, S. Shi, Q. Bao, X. Liu, and M. Fahlman, “Role of Thick-Lithium Fluoride Layer in Energy Level Alignment at Organic/Metal Interface: Unifying Effect on High Metallic Work Functions,” *Adv Mater Interfaces*, vol. 2, no. 4, pp. 1–8, 2015, doi: 10.1002/admi.201400527.

[27] M. Uda, A. Nakamura, T. Yamamoto, and Y. Fujimoto, “Work function of polycrystalline Ag, Au and Al,” *J Electron Spectros Relat Phenomena*, vol. 88–91, pp. 643–648, Mar. 1998, doi: 10.1016/S0368-2048(97)00236-3.

[28] E. W. Cowell, S. W. Muir, D. A. Keszler, and J. F. Wager, “Barrier height estimation of asymmetric metal-insulator-metal tunneling diodes,” *J Appl Phys*, vol. 114, no. 21, p. 213703, Dec. 2013, doi: 10.1063/1.4839695.

[29] S.-G. Nam *et al.*, “Barrier height control in metal/silicon contacts with atomically thin MoS_2 and WS_2 interfacial layers,” *2d Mater*, vol. 5, no. 4, p. 041004, Aug. 2018, doi: 10.1088/2053-1583/aad794.

[30] R. Kronig and W. G. Penney, “Quantum mechanics of electrons in crystal lattices,” *Proceedings of the Royal Society of London. Series A, Containing Papers of a Mathematical and Physical Character*, vol. 130, no. 814, pp. 499–513, Feb. 1931, doi: 10.1098/rspa.1931.0019.

[31] J. A. Appelbaum and D. R. Hamann, “PHYSICAL REVIEW B Surface-induced charge disturbances in filled bands,” 1974. doi: 10.1103/physrevb.10.4973.

[32] F. Marsiglio and R. L. Pavelich, “The tight-binding formulation of the Kronig-Penney model,” *Sci Rep*, vol. 7, no. 1, Dec. 2017, doi: 10.1038/s41598-017-17223-2.

[33] E. Kaxiras, *Atomic and Electronic Structure of Solids*. Cambridge University Press, 2003. doi: 10.1017/CBO9780511755545.

[34] P. W. Peacock and J. Robertson, “Band offsets and Schottky barrier heights of high dielectric constant oxides,” *J Appl Phys*, vol. 92, no. 8, pp. 4712–4721, Oct. 2002, doi: 10.1063/1.1506388.

[35] J. Robertson, “Band offsets, Schottky barrier heights, and their effects on electronic devices,” *Journal of Vacuum Science & Technology A: Vacuum,*

Surfaces, and Films, vol. 31, no. 5, p. 050821, Sep. 2013, doi: 10.1116/1.4818426.

[36] "J. J. Sakurai, Jim J. Napolitano - Modern Quantum Mechanics (2nd Edition)-Addison Wesley (2010) (2)".

[37] R. G. Forbes, "On the need for a tunneling pre-factor in Fowler–Nordheim tunneling theory," *J Appl Phys*, vol. 103, no. 11, p. 114911, Jun. 2008, doi: 10.1063/1.2937077.

[38] J. Frenkel, "On Pre-Breakdown Phenomena in Insulators and Electronic Semi-Conductors." doi: 10.1103/PhysRev.54.647.

[39] R. G. Forbes, "Comments on the continuing widespread and unnecessary use of a defective emission equation in field emission related literature," *J Appl Phys*, vol. 126, no. 21, p. 210901, Dec. 2019, doi: 10.1063/1.5117289.

[40] T. Hatakeyama and T. Shinohe, "Reverse characteristics of a 4H-SiC schottky barrier diode," in *Materials Science Forum*, 2002, vol. 389–393, pp. 1169–1172. doi: 10.4028/www.scientific.net/MSF.389-393.1169.

[41] H. Okino, N. Kameshiro, K. Konishi, A. Shima, and R. I. Yamada, "Analysis of high reverse currents of 4H-SiC Schottky-barrier diodes," *J Appl Phys*, vol. 122, no. 23, Dec. 2017, doi: 10.1063/1.5009344.

[42] L. Lin, Y. Guo, and J. Robertson, "Metal silicide Schottky barriers on Si and Ge show weaker Fermi level pinning," *Appl Phys Lett*, vol. 101, no. 5, Jul. 2012, doi: 10.1063/1.4742861.

[43] T. Nishimura, T. Yajima, and A. Toriumi, "Reexamination of Fermi level pinning for controlling Schottky barrier height at metal/Ge interface," *Applied Physics Express*, vol. 9, no. 8, Aug. 2016, doi: 10.7567/APEX.9.081201.

[44] K. Hirose, Ohdomari, and M. Uda, “Schottky-barrier heights of transition-metal-silicide-silicon contacts studied by x-ray photoelectron spectroscopy measurements,” *Phys Rev B*, vol. 37, no. 12, 1988.

[45] T. Nishimura, X. Luo, S. Matsumoto, T. Yajima, and A. Toriumi, “Almost pinning-free bismuth/Ge and /Si interfaces,” *AIP Adv*, vol. 9, no. 9, Sep. 2019, doi: 10.1063/1.5115535.

[46] B. Mereu, C. Rossel, E. P. Gusev, and M. Yang, “The role of Si orientation and temperature on the carrier mobility in metal oxide semiconductor field-effect transistors with ultrathin HfO 2 gate dielectrics,” *J Appl Phys*, vol. 100, no. 1, 2006, doi: 10.1063/1.2210627.

[47] C. A. Mead, “Surface states on semiconductor crystals; Barriers on the Cd(Se:S) system,” *Appl Phys Lett*, vol. 6, no. 6, pp. 103–104, 1965, doi: 10.1063/1.1754185.

[48] W. Shockley, “On the Surface States Associated with a Periodic Potential,” 1939.

[49] S. Kurtin, T. C. Mcgill, and C. A. Mead, “PHYSICAL REVIEW LETTERS FUNDAMENTAL TRANSITION IN THE ELECTRONIC NATURE OF SOLIDS*,” 1969.

[50] Linus Pauling, “THE NATURE OF THE CHEMICAL BOND. APPLICATION OF RESULTS OBTAINED FROM THE QUANTUM MECHANICS AND FROM A THEORY OF PARAMAGNETIC SUSCEPTIBILITY TO THE STRUCTURE OF MOLECULES,” UTC, 1931. doi: 10.1021/ja01355a027.

[51] C. R. A. Catlow and A. M. Stoneham, “Phys. C: Solid State Phys. 16 4321 J. Phys. C: Solid State Phys., 16 (1983) 43214338,” 1983. [Online]. Available: http://iopscience.iop.org/0022-3719/16/22/010

[52] A. R. Miedema, “THE ELECTRONEGATIVITY PARAMETER FOR TRANSITION METALS: HEAT OF FORMATION AND CHARGE TRANSFER IN ALLOYS,” Elsevier Sequoia S.A, 1973.

[53] J. C. Phillips, *Bonds and Bands in Semiconductors*. Elsevier, 1973. doi: 10.1016/B978-0-12-553350-8.X5001-5.

[54] C. Falter, W. Ludwig, M. Selmke, and W. Zierau, “AN ALTERNATIVE DEFINITION OF IONICITY ON A MICROSCOPIC SCALE,” 1984.

[55] J. Tersoff, “Schottky barriers and semiconductor band structures,” *Phys Rev B*, vol. 32, no. 10, pp. 6968–6971, 1985, doi: 10.1103/PhysRevB.32.6968.

[56] C. K. Perkins *et al.*, “Demonstration of Fowler-Nordheim Tunneling in Simple Solution-Processed Thin Films,” *ACS Appl Mater Interfaces*, vol. 10, no. 42, pp. 36082–36087, Oct. 2018, doi: 10.1021/acsami.8b08986.

[57] W. Weiss, H. D. Wiemhofer, and W. Gopel, “Role of ionic defects at semiconductor-insulator interfaces: Spectroscopic results on CaFz/InP(001) and SrF2/InP(001) structures.”

[58] D. Mao, K. Young, A. Kahn, R. Zanoni, J. Mckinley, and G. Margaritondo, “Photoemission study of CaF2-and SrF2-GaAs(110) interfaces formed at room temperature.”

[59] K. Young, S. Horng, A. Kahn, and J. M. Phillips, “711) GaAs SURFACES,” AND.

[60] S. Sinharoy, “HETEROEPITAXIAL STRUCTURE RESEARCH : A REVIEW,” 1990.

[61] B. Brennan, S. McDonnell, and G. Hughes, “Photoemission studies of the interface formation of ultrathin MgO dielectric layers on the oxidised Si(111) surface,” *J Phys Conf Ser*, vol. 100, no. 4, p. 042047, Mar. 2008, doi: 10.1088/1742-6596/100/4/042047.

[62] K. W. Wong, Y. M. Wang, S. T. Lee, and R. W. M. Kwok, “Lowering of work function induced by deposition of ultra-thin rubidium fluoride layer on polycrystalline diamond surface.”

[63] R. Schlaf *et al.*, “Photoemission spectroscopy of LiF coated Al and Pt electrodes,” *J Appl Phys*, vol. 84, no. 12, pp. 6729–6736, Dec. 1998, doi: 10.1063/1.369000.

[64] Y. M. Wang *et al.*, “Recent studies on diamond surfaces,” *Diam Relat Mater*, vol. 9, no. 9, pp. 1582–1590, 2000, doi: 10.1016/S0925-9635(00)00292-2.

[65] Y. Frenkel, *Kinetic Theory of Liquids*. Clarendon Press, 1946.

[66] L. E. Smart and E. A. Moore, *Solid State Chemistry*, 4th ed. CRC Press, 2016. doi: 10.1201/b12047.

[67] W. Bollmann, P. Görlich, W. Hauk, and H. Mothes, “Ionic conduction of pure and doped CaF2 and SrF2 crystals,” *Physica Status Solidi (a)*, vol. 2, no. 1, pp. 157–170, May 1970, doi: 10.1002/pssa.19700020120.

[68] M. J. Gillan and P. W. M. Jacobs, “Entropy of a point defect in an ionic crystal,” *Phys Rev B*, vol. 28, no. 2, pp. 759–777, Jul. 1983, doi: 10.1103/PhysRevB.28.759.

[69] J. H. Harding, “Calculation of the entropy of defect processes in ionic solids,” *Journal of the Chemical Society, Faraday Transactions 2*, vol. 85, no. 5, p. 351, 1989, doi: 10.1039/f29898500351.

[70] R. SMoLUcHowsKI, “Anisotropy of the Electronic Work Function of Metals,” 1936.

[71] M. C. Barnes, D.-Y. Kim, H. S. Ahn, C. O. Lee, and N. M. Hwang, “Deposition mechanism of gold by thermal evaporation: approach by charged cluster model,” 2000.

[72] M. Ohring, “Thin-Film Evaporation Processes,” in *Materials Science of Thin Films*, Elsevier, 2002, pp. 95–144. doi: 10.1016/B978-012524975-1/50006-9.

[73] H. Fujiwara, *Spectroscopic Ellipsometry*. John Wiley and Sons, Ltd, 2007.

[74] H. H. Li, “Refractive index of alkali halides and its wavelength and temperature derivatives,” *J Phys Chem Ref Data*, vol. 5, no. 2, pp. 329–528, Apr. 1976, doi: 10.1063/1.555536.

[75] E. D. Palik, *Handbook of Optical Constants of Solids*, vol. 2. Academic Press, 1991.

[76] M. van Rijnbach, R. J. E. Hueting, M. Stodolny, G. Janssen, J. Melskens, and J. Schmitz, “On the Accuracy of the Cox–Strack Equation and Method for Contact Resistivity Determination,” *IEEE Trans Electron Devices*, vol. 67, no. 4, pp. 1757–1763, Apr. 2020, doi: 10.1109/TED.2020.2974194.

[77] F. Feldmann *et al.*, “Charge carrier transport mechanisms of passivating contacts studied by temperature-dependent J-V measurements,” *Solar Energy Materials and Solar Cells*, vol. 178, no. October 2017, pp. 15–19, 2018, doi: 10.1016/j.solmat.2018.01.008.

[78] W. Wang *et al.*, “An Expanded Cox and Strack Method for Precise Extraction of Specific Contact Resistance of Transition Metal Oxide/ *n*-Silicon Heterojunction,” *IEEE J Photovolt*, vol. 9, no. 4, pp. 1113–1120, Jul. 2019, doi: 10.1109/JPHOTOV.2019.2917386.

[79] S. M. Sze, C. R. Crowell, and D. Kahng, “Photoelectric determination of the image force dielectric constant for hot electrons in Schottky barriers,” *J Appl Phys*, vol. 35, no. 8, pp. 2534–2536, 1964, doi: 10.1063/1.1702894.

[80] S. Chander, A. Purohit, A. Nehra, S. P. Nehra, and M. S. Dhaka, “A Study on Spectral Response and External Quantum Efficiency of Mono-Crystalline

Silicon Solar Cell," *International Journal of Renewable Energy Research*, no. v5i1, 2015, doi: 10.20508/ijrer.v5i1.1760.g6469.

[81] V. Palomares, P. Serras, I. Villaluenga, K. B. Hueso, J. Carretero-González, and T. Rojo, "Na-ion batteries, recent advances and present challenges to become low cost energy storage systems," *Energy Environ Sci*, vol. 5, no. 3, p. 5884, 2012, doi: 10.1039/c2ee02781j.

[82] L. Wang *et al.*, "Rhombohedral Prussian White as Cathode for Rechargeable Sodium-Ion Batteries," *J Am Chem Soc*, vol. 137, no. 7, pp. 2548–2554, Feb. 2015, doi: 10.1021/ja510347s.

[83] X. Wang *et al.*, "Ultra-stable all-solid-state sodium metal batteries enabled by perfluoropolyether-based electrolytes," *Nat Mater*, Jul. 2022, doi: 10.1038/s41563-022-01296-0.

[84] D. K. Lee, S. Kim, S. Oh, J.-Y. Choi, J.-L. Lee, and H. K. Yu, "Water-Soluble Epitaxial NaCl Thin Film for Fabrication of Flexible Devices," *Sci Rep*, vol. 7, no. 1, p. 8716, Dec. 2017, doi: 10.1038/s41598-017-09603-5.

[85] P. Zaumseil, "High-resolution characterization of the forbidden Si 200 and Si 222 reflections," *J Appl Crystallogr*, vol. 48, pp. 528–532, Apr. 2015, doi: 10.1107/S1600576715004732.

[86] J. Bullock *et al.*, "Lithium Fluoride Based Electron Contacts for High Efficiency n-Type Crystalline Silicon Solar Cells," *Adv Energy Mater*, vol. 6, no. 14, Jul. 2016, doi: 10.1002/aenm.201600241.

[87] S. Wan *et al.*, "Schottky contact formation by an insulator: Lithium fluoride on silicon," *Appl Phys Lett*, vol. 118, no. 24, Jun. 2021, doi: 10.1063/5.0049272.

[88] F. Wu, H. Wang, Y. C. Shen, and H. Jiang, "Electronic properties of ionic surfaces: A systematic theoretical investigation of alkali halides," *Journal of Chemical Physics*, vol. 146, no. 1, Jan. 2017, doi: 10.1063/1.4973316.

[89] M. Piacentini, “A new interpretation of the fundamental exciton region in LiF,” *Solid State Commun*, vol. 17, no. 6, pp. 697–700, Sep. 1975, doi: 10.1016/0038-1098(75)90388-9.

[90] P. Zhang and T. Pan, “Exact analytical theory for inverse tunneling of free vacuum electrons into a solid,” *AIP Adv*, vol. 7, no. 6, Jun. 2017, doi: 10.1063/1.4986220.

[91] P. Paramahans Manik *et al.*, “Fermi-level unpinning and low resistivity in contacts to n-type Ge with a thin ZnO interfacial layer,” *Appl Phys Lett*, vol. 101, no. 18, p. 182105, Oct. 2012, doi: 10.1063/1.4764909.

[92] C. A. Gilbert, S. D. Kenny, R. Smith, and E. Sanville, “Ab initio study of point defects in magnesium oxide,” *Phys Rev B Condens Matter Mater Phys*, vol. 76, no. 18, Nov. 2007, doi: 10.1103/PhysRevB.76.184103.

[93] J. Chen, Z. Zhang, Y. Guo, and J. Robertson, “Schottky barrier heights of defect-free metal/ZnO, CdO, MgO, and SrO interfaces,” *J Appl Phys*, vol. 129, no. 17, May 2021, doi: 10.1063/5.0047447.

[94] W. J. Zhu, T.-P. Ma, T. Tamagawa, J. Kim, and Y. Di, “Current Transport in Metal/Hafnium Oxide/Silicon Structure,” 2002.

[95] S. Gupta, P. Paramahans Manik, R. Kesh Mishra, A. Nainani, M. C. Abraham, and S. Lodha, “Contact resistivity reduction through interfacial layer doping in metal-interfacial layer-semiconductor contacts,” *J Appl Phys*, vol. 113, no. 23, p. 234505, Jun. 2013, doi: 10.1063/1.4811340.

[96] Y. Liu *et al.*, “A novel passivating electron contact for high-performance silicon solar cells by ALD Al-doped TiO2,” *Solar Energy*, vol. 228, pp. 531–539, Nov. 2021, doi: 10.1016/j.solener.2021.09.083.

[97] M. M. Shehata *et al.*, “Outstanding Surface Passivation for Highly Efficient Silicon Solar Cells Enabled by Innovative Al_yTiO_x/TiO_x Electron-

Selective Contact Stack," *Solar RRL*, p. 2200550, Aug. 2022, doi: 10.1002/solr.202200550.